Epithelial Plasticity and Innate Immune Activation Promote Lung Tissue Remodeling following Respiratory Viral Infection.

Andrew K. Beppu[1,2,3*], Juanjuan Zhao[1,2,3*], Changfu Yao[1,2,3], Gianni Carraro[1,2,3], Edo Israely[3], Anna Lucia Coelho[1,2], Cory M Hogaboam[1,2], William C. Parks[1,2], Jay K. Kolls[4], Barry R. Stripp[1,2,3#]

[1]Women's Guild Lung Institute, Department of Medicine, Cedars-Sinai Medical Center, Los Angeles, CA 90048, USA.

[2]Division of Pulmonary and Critical Care Medicine, Department of Medicine, Cedars-Sinai Medical Center, Los Angeles, CA 90048, USA.

[3]Regenerative Medicine Institute, Department of Medicine, Cedars-Sinai Medical Center, Los Angeles, CA 90048, USA.

[4] Center for Translational Research in Infection and Inflammation Tulane School of Medicine

*** Co-first authors**

 # Corresponding author: Barry R. Stripp (barry.stripp@csmc.edu**)**

The authors have declared that no conflict of interest exists.

Summary:

Epithelial plasticity has been suggested in lungs of mice following genetic depletion of stem cells but is of unknown physiological relevance. Viral infection and chronic lung disease share similar pathological features of stem cell loss in alveoli, basal cell (BC) hyperplasia in small airways, and innate immune activation, that contribute to epithelial remodeling and loss of lung function. We show that a novel lineage of distal airway secretory cells, intralobar serous (IS) cells, are activated to assume BC fates following influenza virus infection. Nascent BC differ from pre-existing BC by high expression of IL-22ra1 and undergo IL-22-dependent expansion for colonization of injured alveoli. Resolution of virus-elicited inflammation resulted in BC>IS re-differentiation in repopulated alveoli, and increased local expression of antimicrobial factors, but failed to replace normal alveolar epithelium. Epithelial plasticity therefore protects against mortality from acute respiratory viral infection but results in distal lung remodeling and loss of lung function.

Introduction:

Stem cell plasticity contributes to tissue regeneration and includes a range of processes such as lineage conversion and de-differentiation of specialized progenitor cells (Blanpain and Fuchs, 2014) . Although epithelial cell plasticity in lung repair has been inferred from lineage tracing and targeted cell ablation studies (Tata et al., 2013; Tata and Rajagopal, 2017), the physiological relevance in lung disease is unknown. The epithelial linings of airways and alveoli are maintained by distinct regional facultative stem/progenitor cells whose progeny include both self-renewing and differentiating subsets (Hogan et al., 2014; Rackley and Stripp, 2012). Regional differences in the fate of differentiating progeny allow for maintenance of locally specialized epithelial functions, such as mucociliary clearance and host defense in the conducting airways and gas exchange in the distal respiratory units. Restriction of progenitor cells and their differentiating progeny to distinct anatomic zones during homeostatic tissue maintenance are necessary for functional integration of these compartments along the proximodistal axis and preservation of normal physiological lung function. However, acute lung injury and chronic lung disease disrupt normal progenitor cell compartmentalization leading to aberrant tissue remodeling and declining lung function. Such is the case following infections by respiratory viruses such as H1N1 influenza A or SARS-CoV2, and in chronic lung diseases such as idiopathic pulmonary fibrosis (IPF). In such conditions, basal cell (BC) hyperplasia in airways leads to the recruitment and colonization of these cells into injured alveolar areas, and this proximalization of distal lung tissue contributes to potentially life-threatening loss of alveolar diffusion capacity (Seibold et al., 2013; Vaughan et al., 2015; Xu et al., 2016; Zuo et al., 2015). However, the identity of epithelial progenitor cells that contribute to proximalization of distal lung tissue and the mechanisms that regulate their fate during tissue remodeling remain poorly defined.

Mirroring what occurs in injured or injected human lungs, acute lung injury in mice infected with a mouse-adapted Puerto Rico 8 (PR8) variant of H1N1 influenza virus is accompanied by BC expansion in airways that ultimately replaces the injured epithelium of the alveolar gas-exchange region (Kumar et al., 2011; Vaughan et al., 2015; Zuo et al., 2015). Even though basal and club cells serve as stem cells for maintenance of the pseudostratified epithelium of proximal airways and cuboidal epithelium of distal airways, respectively, lineage tracing studies suggest that hyperplastic BC appearing in distal lung tissue of PR8-infected mice are derived from neither of these canonical stem cell populations (Ray et al., 2016; Vaughan et al., 2015; Zuo et al., 2015). Instead, PR8-elicited BC (hereon referred to as nascent BC) derive from alternate small airway progenitors that can be lineage traced based upon expression of either Sox2 or p63 transcription factors (Ray et al., 2016; Xi et al., 2017; Yang et al., 2018). Similarly, in proximal airways, a-smooth muscle actin-expressing myoepithelial cells of submucosal glands (SMG) or SSEA4-expressing secretory cell progeny of basal cells can replenish basal stem cells following injury (Tata et al., 2018; Tata et al., 2013). However, the

molecular and functional relationship between epithelial progenitors of SMG or upper airway surface epithelium that can replace local basal stem cells – versus those that yield expanding BC in small airways following PR8 infection – remain to be established.

Although much is known of mechanisms that regulate the renewal and fate of BC within pseudostratified airways, mechanisms regulating hyperplastic BC appearing in alveolar epithelium of PR8-infected mice are poorly defined. Evidence of roles for local hypoxia (Xi et al., 2017) and the altered inflammatory milieu (Katsura et al., 2019; Pociask et al., 2013; Tavares et al., 2017) that accompanies PR8 infection suggest potential roles for innate immune activation as a regulator of BC fate and epithelial remodeling. Epithelial-immune crosstalk serves as a critical regulator of progenitor cell function in multiple organs including the lung, gut, and skin (Aparicio-Domingo et al., 2015; Barrow et al., 2018; Boniface et al., 2005; Kempski et al., 2017; Lindemans et al., 2015). Here, we show that the unique origins and molecular phenotype of nascent BC elicited by PR8 infection allows for their dynamic response to the activated innate immune system. Interleukin 22 derived from locally activated γδT cells promotes self-renewal and hyperplasia of BC within alveolar epithelium that ultimately assume serous cell fates in previously injured regions during resolution of the PR8-elicited inflammatory response. This remodeling response to respiratory viral infection allows for efficient replacement of exposed basement membrane in the injured alveolar epithelium and local production of an antibacterial secretome to protect against secondary bacterial infection.

Results:

Activation and expansion of intralobular serous (IS) cells precedes BC hyperplasia following influenza-induced acute lung injury.

BC hyperplasia occurs in airways of patients with chronic lung disease and in lung tissue of those succumbing to acute respiratory viral infections such as H1N1 influenza virus or COVID-19 (Davis and Wypych, 2021; Fang et al., 2020; Rock et al., 2010; Vaughan et al., 2015; Zuo et al., 2015). Based on lineage tracing studies, the majority of cells in mouse lungs that acquire BC fates in response to influenza virus-induced acute lung injury have been proposed to arise from immature $P63^{+}Krt5^{-}$ basal progenitors (Xi et al., 2017; Yang et al., 2018). However, a significant fraction of nascent BC seen during injury failed to retain a P63 lineage tag suggesting the presence of other contributing non-basal progenitors (Fernanda de Mello Costa et al., 2020). We sought to interrogate the existence of non-canonical progenitors by assessing dynamic changes in epithelial cell populations in response to influenza-induced acute lung injury. We generated a comprehensive profile of single cell transcriptomes for epithelial cells isolated from trachea, extrapulmonary bronchus, intralobar airways and alveolar regions of control C57Bl/6 mice (Day 0) and of mice infected and recovering from exposure to the PR8 strain of H1N1 influenza virus (Day 3-240; Fig. 1A, B). Results displayed as uniform manifold approximation and projection (UMAP) two-dimensional plots reveal eight major cell clusters that were categorized according to known lung epithelial cell types based upon their unique gene expression signatures (Fig. 1B, C, Supp. Fig. 1A). Even though each of the major cell types were observed among epithelial cells sampled from all control and post-exposure time points, their relative proportions within total sampled epithelial cells showed significant variability (Fig. 1 D).

BC were rare among epithelial cells sampled from lobes of control mice or mice at 3-9 days post PR8 infection but showed progressive increases in representation thereafter (Fig. 1D, E). Serous cells were the only other rare epithelial cell type in lung lobes of naïve mice whose abundance increased following PR8 infection (Fig. 1D, E). However, the increase in representation of serous cells preceded increases in BC representation among epithelial cells sampled across the time course (Fig. 1D). Furthermore, serous cells observed in the PR8-exposed lung included a subset with ectopic expression of BC marker genes *Trp63*, *Krt14* and *Krt5* in all post-exposure recovery time points compared to serous cells observed in airways of naïve mice (Fig. 1F). Interestingly, expanding populations of serous cells observed during recovery following PR8 infection were unique among distal lung epithelial cell types in their expression of genes involved in anti-microbial host defense, such as *Ifitm1*, *Ifitm3*, *Bpifa1*, and *Ltf* (Supp. Fig. 1B). Expansion of this serous population coupled with acquisition of a transcriptome that shares similarities with nascent airway BC during recovery

from PR8 exposure, led us to speculate that rare airway serous cells represent the progenitor cell-of-origin for nascent BC observed in airways and alveolar epithelium of infected mice.

Because serous cells show increased representation in single cell data sets at earlier stages in the response to PR8 infection, we speculated that serous cells represent the progenitor cell type accounting for nascent BC. To explore further the molecular phenotype of serous cells that appear early in the airway response to PR8 infection, we utilized our single cell dataset to identify candidate differentially expressed genes (DEGs) that discriminate serous cells from other epithelial cell types in conducting airways. Despite many similarities in the gene expression signatures between club and serous cells, unsupervised clustering of these epithelial populations was unaffected by regression of cell cycle genes (Supp. Fig. 1C, D, E). We found that serous cells express high levels of *Scgb3a2*, as do club cells, but that unlike club cells they lack expression of *Scgb1a1*. Furthermore, antimicrobial factors, such as *Bpifa1* and *Ltf*, whose expression defines serous cells of proximal airways and submucosal glands (Tata et al., 2018), were significantly elevated in serous cells compared to club cells of the PR8 injured lung (Fig. 1G, Supp. Fig. 2A). Immunofluorescence labeling revealed that a small fraction of intralobular Scgb3a2-positive cells were also positive for Msln and Bpifa1, indicating the presence of serous populations within the lower respiratory tract, herein called intralobular serous (IS) cells (Fig. 1H).

Transcriptome analysis predicts IS>basal plasticity during recovery from PR8 infection.

To further examine the potential for IS cells to serve as progenitors for expansion of nascent BC, we used gene set enrichment to identify DEGs among these epithelial cell clusters at different times post-PR8 infection. We observed a significant induction of gene sets associated with cell cycle at 5- and 7-days post infection coinciding with the appearance of proliferating conducting airway epithelium observed *in vivo* (Fig. 2A). However, we observed enrichment of cell-cycle gene-sets at these time points only in serous and BC with little to no enrichment of these gene sets in other major cell types of conducting airways (Fig. 2A).

We used our scRNAseq dataset to interrogate lineage relationships between BC, IS cells, and other airway secretory cell populations. Transcript splicing was assessed by Velocyto (La Manno et al., 2018) to predict differentiation trajectories among IS cells, club cells, and nascent BC during early (naïve-day 11) and late (day 14-day 240) responses to PR8 infection (Fig. 2B, C). Computational analysis of cell fate dynamics predicted a process that IS cells de-differentiated into BC at early time points post-PR8 infection (Fig. 2C). In contrast, trajectory analysis predicted the transition of BC back to IS cells at late recovery time points (Fig. 2C).

We next used Visium spatial RNA-Seq to define the relationship between nascent BC and IS cells within lung tissue 14 days after PR8 infection (Fig. 2D). Unsupervised clustering revealed 7 transcriptionally distinct gene signatures that were projected onto a spatial map of the sampled tissue

section (Fig. 2E-G). Cell type signature scores generated from scRNAseq (Fig. 1C) were applied to spatial RNAseq data to colocalize cell types (Fig. 2H). The resulting spatial maps of cell types demonstrated close spatial association between nascent BC and IS cells, but not nascent BC and club cells, as suggested from the predicted lineage relationships between these cell types by RNA velocity analysis. We corroborated close spatial localization of nascent BC and IS cells predicted from spatial transcriptome profiling by immunofluorescent localization of Scgb3a2 to regions of Krt5-immunoreactivity within remodeled regions of alveolar epithelium of PR8-infected mice (Fig. 2I-K).

Scgb3a2^{pos}Scgb1a1^{neg} IS cells demonstrate serous-basal-serous plasticity during repair following PR8

We developed a lineage tracing approach to independently define the contribution of IS cells and club cells towards BC expansion after PR8 infection. Our single-cell and spatial RNAseq data indicated that both IS cells and club cells express Scgb3a2 but that only club cells express Scgb1a1. Based upon these data, we generated dual recombinase (DR) mice harboring a Dre/Cre reporter allele in conjunction with *Scgb1a1-CreER* and *Scgb3a2-DreER* recombinase driver alleles (Fig. 3A). Tamoxifen (TM) exposure of these mice results in Dre-mediated excision of a poly A signal (STOP) within Scgb3a2-expressing IS and club cells, with subsequent Cre-mediated excision of tdT-STOP within Scgb1a1-expressing club cells. Outcomes of these recombination events are tracing of Scgb3a2^{+}/Scgb1a1^{-} IS cells by expression of tdT (Lin^{3a2}), and Scgb3a2^{+}/Scgb1a1^{+} club cells by expression of eGFP (Lin$^{3a2/1a1}$; Fig. 3A). Tamoxifen exposure was followed by a wash-out period of 9 days before analysis of lineage tracing in lungs of naïve mice (Fig. 3B). Lineage labeling of Scgb3a2 immunoreactive cells in airways of naïve mice was determined to be 75.2 ± 3.06%, of which Lin^{3a2} IS cells (16.8% of total lineage-labeled cells) were interspersed among Lin$^{3a2/1a1}$ club cells (83.2% of total lineage-labeled cells) (Fig. 3 C, D, I). We detected expression of the serous cell marker Bpifa1 only within tdT lineage traced cells, which were negative for markers of ciliated and BC types in airways of naïve mice (Fig. 3D.).

We next sought to assess the contribution of Lin^{3a2} cells to epithelial remodeling and BC expansion following PR8 infection. TM-treated 3a2/1a1 DR mice were infected with PR8 influenza virus and examined at 7, 14 or 21 days (Fig. 3B). Expanding populations of Krt5^{+} BC were identified in airways 7 days after PR8 infection (Fig. 3E, Supp. Fig. 3A). Dual immunofluorescence for lineage reporters and the BC marker Krt5 revealed basal-like cells that included Lin^{3a2}-positive/high, -positive/low and -negative subsets (Fig. 3F, J). Although Lin$^{3a2/1a1}$-positive epithelial cells were detected, no immunofluorescent colocalization was seen between eGFP and Krt5. These observations are consistent with reports by others and us that club cells do not contribute significantly to the expanding pool of BC in response to lung injury or infection (Ray et al., 2016; Vaughan et al., 2015).

Further expansion of Lin^{3a2}-high and -low epithelial cells was apparent at 14 days after PR8 infection, at which time Lin^{3a2}-low/Krt5 dual-positive epithelial cells were also observed in regions of basal hyperplasia localized within injured alveolar epithelium (Fig. 3E). Nascent Krt5-immunoreactive basal-like cells displayed a Lin^{3a2}-low phenotype at recovery day 14 and beyond, whereas Lin^{3a2}-high epithelial cells were predominantly of a Krt5-negative immunophenotype and occupied a suprabasal/luminal location within the repairing airway epithelium (Fig. 3E). Expanding Lin^{3a2}-high cells displayed characteristics of IS cells and show increasing abundance with time of recovery after PR8 infection that validate observations made by scRNAseq (Fig. 1E). Interestingly, injured alveolar regions that were repopulated by basal-like Krt5-positive/Lin^{3a2}-low cells at day 14 post-infection showed greater heterogeneity at recovery day 21 (Fig. 3G, K). By recovery day 21, Lin^{3a2}-positive cells occupying alveolar regions included both Krt5-positive/ Lin^{3a2}-low and Krt5-negative/ Lin^{3a2}-high patches, with some patches appearing to show transitional phenotypes suggestive of transitioning cell states (Fig. 3G). These data are consistent with trajectory analysis of scRNAseq data suggesting that nascent basal-like cells that expand after PR8 infection eventually transition back to IS cells (Fig. 2C). Immunofluorescence staining for Scgb3a2 confirmed the IS cell phenotype of alveolar Krt5-negative/ Lin^{3a2}-high cells (Supp. Fig. 3B). Our data from dual lineage tracing corroborate cellular trajectory predictions that were based on scRNAseq data and suggest that the repairing epithelium is highly dynamic. The changing milieu of the PR8 injured lung contributes to both specification of nascent BC from an airway IS progenitor, followed by their differentiation back to IS cells in airways and injured alveolar regions (Fig. 3H).

Regulatory gene networks involved in immune-epithelial crosstalk are activated in nascent basal but not in IS cells.

Next, defined mechanisms that regulate specification and fate of nascent BC that expand in lungs of PR8 infected mice. To gain further insights into pathways regulating the behavior of either IS or BC, we evaluated changes in regulatory genes over the time course of PR8 infection and recovery using Bigscale2 (Iacono et al., 2019; Iacono et al., 2018). ScRNAseq data from naïve and days 11-17 after PR8 infection were sorted by cell type to yield four regulatory gene networks (GRN) (Fig. 4A). Cell type specific GRNs from post-infection time points were then compared to their respective naïve cell controls to normalize node and edge values (Fig. 4B). A gene list of the top 300 delta degree node centralities was generated and used to identify enriched gene ontology (GO) terms by Panther-based overrepresentation tests (Fig. 4C, D). Gene regulatory networks shown in Fig. 4C demonstrate dynamic changes occurring among BC but less so for IS cells between naïve and post-infection time points. Highly enriched GO terms in basal populations included pathways involving cell proliferation, such as activation of canonical Wnt signaling (Haas et al., 2019) (not shown), consistent with observed BC proliferation (Fig. 2A) and associated hyperplasia (Fig. 1D) that accompanies recovery

from PR8 infection. Pathways associated with cytokine signaling and innate immune stimulation of epithelial cells were also significantly up regulated in BC, and to a lesser extent in IS cells, isolated from PR8 infected lungs (Fig. 4D).

Innate immune activation is a well-documented response to respiratory viral infection in general and is a key regulator of epithelial cell fate leading to remodeling in airways and increased postnatal susceptibility to allergic inflammation (Hackett et al., 2011). Notably, local production of TNFα and IL-1β following influenza virus infection in mice promote the regenerative capacity of alveolar epithelium (Katsura et al., 2019), and IL-22 enhances survival and reduces lung fibrosis following PR8 infection (Pociask et al., 2013). To explore further the potential roles for cytokine-mediated changes in epithelial cell fate, we performed a multiplex protein assay to quantify cytokine responses in lungs of influenza virus infected C57/Bl6 mice. We observed a significant increase in interferon (Ifnγ) and pro-inflammatory cytokines IL-6, TNFα and IL-1β (Fig. 4E; Supp. Fig. 4A) , consistent with known responses to respiratory viral infection (Katsura et al., 2019). A significant induction of type 17-related cytokines, including IL-17a, IL-10 and IL-22, was observed in lung tissue homogenates and/or bronchoalveolar lavage (BAL) of mice between recovery days 5-11 after PR8 infection (Fig. 4E, Supp. Fig. 4A). The protective effects of IL-22 (Pociask et al., 2013) and the coincidence of increased cytokine production with BC expansion in airways and alveoli led us to speculate that IL-22 signaling plays a role in BC expansion following PR8 infection.

Renewal and differentiation of nascent BC is regulated by $\gamma\delta$T-cell derived IL-22.

To further explore roles for innate immune activation and IL-22 in regulation of epithelial cells in the airways and alveoli of PR8 exposed mice, we used scRNAseq to define changes to immune cell populations elicited in response to infection (Fig. 5 A, B). ScRNAseq data were collected from $CD45^+$ lung cells recovered at different times following PR8 infection. UMAP dimensional reduction of aggregated data allowed visualization of three major immune subsets (T, B lymphoid & myeloid) (Fig. 5C, D). Clusters of similar cells were identified and annotated by SingleR (Aran et al., 2019) (Fig. 5E, F). We sought to define spatial context of these major immune subsets in relation to nascent BC observed during recovery. Gene signatures derived from immune enriched scRNAseq dataset (Fig. 5C) were used to infer cell localization within spatial RNAseq data (Fig. 5 G). Spatial gene expression analysis indicates preferential colocalization of T lymphoid subsets with BC-rich regions in recovering lung tissue (Fig. 5G, H, I), of which type 17 $\gamma\delta$T cells show increased abundance at periods of BC hyperplasia (Fig.5J, K, Supp. Fig.4B, C). This led us to consider the possible regulatory influence of T lymphoid cells over BC fate.

Since several immune subsets can secrete IL-22, we generated mice harboring *IL-22^{Cre}/ROSA-26-tdT* to fate map IL-22-lineage immune cells during the repair response to PR8 infection (Fig. 6A). To

identify the cell types expressing IL-22, we gated IL-22 lineage tag (tdT) $CD45^+$ cells for expression of lymphoid markers CD3 and CD4 (Fig. 6B). We found that $CD3^+CD4^-$ γδT cells subsets represented the bulk of IL-22-lineage immune cells elicited in response to PR8 infection, with minor contributions made by $CD3^+CD4^+$ Th17 cells (Fig. 6B, Supp. Fig. 5A). Interestingly, non-T lymphoid $CD3^-$ subsets did not contribute to the IL-22-expressing lineage following PR8 infection (Supp Fig. 5A). Immunofluorescence analysis demonstrated that IL-22-immunoreactive immune cells localize to nascent BC and were induced in response to acute lung injury (Fig. 6C, D).

To identify epithelial cell types capable of responding to IL-22 signaling, we use immunofluorescence to identify which epithelial subsets express IL-22ra1, the subunit of heterodimeric IL-22 receptor that confers ligand specificity to IL-22. Notably, within the conducting airway of naïve mice, the highest level of IL-22ra1 immunoreactivity was observed among post-mitotic ciliated epithelial cells, with little to no immunoreactivity seen on club, basal or serous cells (Fig. 6E). However, a significant level of IL-22ra1 expression was observed in hyperplastic alveolar BC (hereon called pods (Kumar et al., 2011)) during recovery following PR8 infection (Fig. 6F). Interestingly, the intensity of IL-22ra1 staining was greatest within the outer periphery of pod regions indicating altered basal responsiveness to IL-22 during injury (Supp. Fig. 6A). Taken together, our data suggest a process of altered IL-22 responsiveness exclusively among nascent basal populations of the PR8-injured lung that regulate BC fate.

IL-22 promotes self-renewal of nascent BC, allowing hyperplastic expansion in airways and injured alveoli.

To investigate the contribution made by IL-22 in regulation of BC fate after PR8 infection, we used *IL-22*^{Cre} homozygous (IL-22-LOF) and *IL-22ra1*$^{fl/fl}$*/Shh-Cre* (IL-22ra1-cLOF) mice to modulate IL-22 levels and signaling, respectively (Fig. 7A). Compared to their corresponding WT control groups, neither IL-22-LOF nor IL-22ra1-cLOF mice showed significant changes in weight loss, viral gene expression, or loss of parenchymal Pdpn immunofluorescence, following PR8 infection (Supp. Fig. 7A, B, C; Fig. 7B). Next, we assessed expansion of Krt5-immunoreactive BC as a function of damaged area in IL-22-LOF mice following PR8 infection. A reduction in $Krt5^+$ BC hyperplasia was observed in IL-22-LOF mice compared to WT control mice at all time points examined, which reached statistical significance by the day 17 recovery time point (Fig. 7B, C). These data were confirmed by assessing *Krt5* mRNA content within total lung RNA isolated at each timepoint, for which statistically significant declines in *Krt5* mRNA were observed at both 14 day and 17 day recovery time points (Fig. 7D). Similar observations of reduced BC expansion were seen among IL-22ra1-cLOF mice following PR8 infection (Supp. Fig. 7C).

Similarly, in other tissues and carcinomas, IL-22 regulates the proliferative potential of epithelial stem progenitors and tumor cells (Jin et al., 2019). To assess if reduced BC hyperplasia observed in IL-22-

LOF mice was associated with reduced epithelial proliferation, we measured the BC proliferative index by immunofluorescence of Ki67 and Krt5 during recovery following PR8 infection. The Ki67-labeling index of BC observed at 7 days post PR8 infection did not differ between IL-22-LOF, IL-22ra1-cLOF, and their corresponding WT controls (Fig. 7E, F). These data indicate that BC expansion at early time points after PR8 infection occurs in an IL-22-independent manner and are consistent with the observed lack of IL-22ra1-immunoreactivity in airway BC of either naïve control mice or mice at early time points after PR8 infection (Fig. 6E). However, nascent BC observed within airway and alveolar regions of both IL-22-LOF and IL-22ra1-cLOF mice at 14 days post-PR8 infection showed significantly reduced levels of Ki67 staining compared to their corresponding WT controls (Fig. 7E, F). These data indicate that at later recovery time points, IL-22 promotes BC expansion and self-renewal, resulting in maintenance of proliferative potential. All genotypes showed reduced BC Ki67 proliferative indices that did not differ significantly between groups at 21 days post-PR8 infection (Fig. 7E, F). To determine if the lack of IL-22 stimulation impacts the fate of alveolar BC during recovery from PR8 infection, we co-stained pod regions observed in parenchymal tissue of PR8-infected WT and IL-22 LOF mice for BC and IS markers. Interestingly, Krt5-immunoreactive pods observed in lungs of either IL-22-LOF or IL-22ra1-cLOF mice 14 days post-PR8 infection displayed evidence for Scgb3a2 expression that was absent in comparable Krt5-immunoreactive pod structures of wildtype control mice (Fig. 7G). The appearance of pod structures composed of epithelial cells showing colocalization of both Krt5 and Scgb3a2 immunofluorescence is consistent with earlier data showing BC>IS differentiation, and supports the notion that residual Krt5-immunoreactivity reflects the BC origin of differentiating IS cells. To further examine the impact that loss of IL-22 has on BC maturation, scRNAseq profiles were generated for epithelial cells isolated from lungs 21 days after PR8-infection of either IL-22ra1-cLOF mice or their corresponding WT controls (Fig. 7H, I). Reduced BC numbers in lungs of IL-22r1a-cLOF mice compared to WT control mice was confirmed by UMAP clustering (Fig. 7J). A significant decrease in the abundance of epithelial cells expressing BC marker genes, Trp63 and Krt5, was observed among IL-22r1a-cLOF mice compared to their WT controls (Fig. 7K). Collectively, our data suggest that IL-22 functions to promote BC renewal over differentiation and that down regulation of innate immune responses at late time points following PR8 infection with associated reduction in IL-22, serves as a trigger to promote basal to serous cell differentiation.

Discussion:

Basal cell (BC) hyperplasia and colonization of the injured alveolar gas-exchange region are significant determinants of tissue remodeling and morbidity among patients with severe respiratory viral infections and share features of distal lung remodeling in patients with interstitial lung disease. Here we show that nascent BC elicited by infection of the mouse respiratory tract with H1N1 influenza virus (strain PR8) are derived predominantly from a serous cell subset of intralobar secretory cells. Nascent BC were distinguished from pre-existing BC by their relatively immature molecular phenotype and expression of IL-22ra1. Innate immune activation and associated secretion of IL-22 promoted self-renewal of nascent BC in airways and establishment of hyperplastic foci within injured alveoli. Germline loss of IL-22 or conditional loss of IL-22ra1 expression within epithelial cells, limited expansion and promoted premature differentiation of nascent BC into serous cells. These findings establish a novel mechanism that promotes expansion of serous cells and their colonization of injured alveolar epithelium, leading to epithelial remodeling and loss of normal alveolar epithelium following respiratory viral infection.

We provide evidence for the existence of two independent secretory cell lineages within intralobar airways of the mouse lung, club cells and intralobar serous (IS) cells. Previous lineage tracing studies have demonstrated that Scgb1a1-expressing club cells are capable of unlimited self-renewal and replacement of specialized epithelial cell types of bronchiolar airways in mice (Rawlins et al., 2009). However, epithelial cell injury in lungs of PR8 infected mice leads to activation of non-canonical epithelial progenitors leading to BC hyperplasia (Ray et al., 2016; Vaughan et al., 2015; Xi et al., 2017; Yang et al., 2018; Zuo et al., 2015). We show that only the IS subset of secretory cells can assume BC fates in the setting of severe respiratory viral infection, suggesting that IS cells function as a reserve epithelial progenitor that are unlikely to make significant if any contribution to homeostatic epithelial maintenance in distal airways. Expansion of IS cells following influenza virus infection and their phenotypic conversion to nascent BC, suggest an unappreciated role for IS cells in epithelial maintenance and repair following severe injury.

Our findings also shed new light on the biological significance of earlier work by Tata et al., who demonstrated that SSEA$^+$ secretory cells of tracheobronchial airways have the unexpected capacity to replenish basal stem cells in a genetic model of BC ablation (Tata et al., 2013). However, even though IS cells identified in our study function in a similar capacity to SSEA$^+$ secretory cells defined by Tata et al., to yield nascent BC, we show that the fate/stemness of IS-derived BC is dictated by the regional microenvironment. Expansion of IS-derived nascent BC and subsequent differentiation led to proximalization of distal conducting airways through replacement of the normally simple cuboidal bronchiolar epithelium with a pseudostratified epithelium, thus demonstrating their multipotency in the airway microenvironment like that described for SSEA$^+$ secretory cell-derived BC in the Tata et al.,

study. Furthermore, nascent BC colonizing injured alveolar regions underwent significant proliferative expansion leading to localized BC hyperplasia, followed by differentiation into IS cells that replaced normal alveolar epithelium with a dysplastic serous cell predominant epithelial lining. It is possible that the observed influence of microenvironment on fate of IS-derived BC following PR8 infection may simply reflect the broader injury elicited by viral infection in our study compared to that resulting from targeted ablation of resident BC in tracheobronchial airways as in the study by Tata and colleagues. However, PR8 infection of mice is more akin to the type of lung injury seen in patients with respiratory viral infection and wide-spread lung injury that accompanies chronic lung disease. Importantly, our data provide insights into mechanisms of epithelial remodeling observed in distal lung tissue of patients with idiopathic pulmonary fibrosis, where alveolar epithelial progenitor cell dysfunction is associated with BC hyperplasia in small airways and establishment of dysplastic cysts in place of normal alveolar epithelium (Carraro et al., 2020; Seibold et al., 2013; Xu et al., 2016).

Even though nascent BC elicited by PR8 influenza virus infection share many properties of pre-existing BC of pseudostratified airways, their immature molecular phenotype and unique expression of IL-22ra1 impart distinctive functional properties that promote rapid epithelial replacement in airways and alveoli. We found that IL-22-expressing $\gamma\delta$T-cells are recruited to sites of PR8-induced airway and alveolar injury, and that their local production of IL-22 promoted self-renewal of nascent BC with no impact on either their specification in airways or migration to injured alveoli. Notably, either germline loss of IL-22 or conditional loss of IL-22ra1 within lung endoderm resulted in premature differentiation of alveolar BC into Scgb3a2^{+} serous cells, thus limiting BC hyperplasia. These data shed new light on mechanisms of fibrosis in lungs of IL-22$^{-/-}$ mice following PR8 infection (Pociask et al., 2013), where IL-22 restrains nascent BC in a highly proliferative and migratory state allowing expansion and re-epithelialization of injured airways and alveoli. We propose a model in which IS cells ultimately colonize injured alveoli following PR8 infection through a combination of IS>BC>IS phenotypic plasticity. Interestingly, these roles for IL-22 in regulating PR8-elicited BC in the lung are in contrast to observations made in other organ systems, such as in the epidermis where IL-22 regulates fibroproliferative responses associated with wound closure (McGee et al., 2013) and in the intestine, where IL-22 regulates epithelial cell fate and host defense through induction of antimicrobial factors (Lo et al., 2019; Zheng et al., 2008). We attribute this differences in outcome to target cells that respond to local production of IL-22 and to the impact of non-cell-autonomous influences of IL-22 signaling within epithelial and stromal cell types. Interestingly, in prior studies IL-22 has been shown to protect against influenza virus-induced pneumonia (Hebert et al., 2020) and has been implicated in the production of antimicrobial factors that protect against secondary bacterial subsequent to influenza virus infection (Abood et al., 2019). Our data demonstrate that these effects are an indirect consequence of IL-22-mediated expansion of IS-derived BC followed by their re-differentiation to yield

IS hyperplasia and provide novel insights into mechanisms of protection against secondary bacterial pneumonia after respiratory viral infection.

Acknowledgments:

We would like to thank Matt Kostelny, Guangzhu Zhang and Katherine Drake for assistance with animal husbandry, and Stephen Beil for general laboratory support. We acknowledge support from the Applied Genomics, Flow Cytometry & Cell Sorting, and Mouse Genetics cores at Cedars Sinai Medical Center (CSMC). This research was supported by grants from the National Institutes of Health (NIH) (R01 HL135163; P01 HL108793) to BRS, by the Bram and Elain Goldsmith Chair in Gene Therapeutics Research, and by the Office of Graduate Education at CSMC.

Author contributions:

Conceptualization, A.K.B., B.R.S.; methodology, A.K.B., J.Z., C.Y., G.C., E.I., A.L.C., B.R.S; data analysis, A.K.B., B.R.S; investigation, A.K.B., J.Z., C.Y., B.R.S; resources, E.I., A.L.C., C.M.H., J.K., B.R.S.; writing – original draft, A.K.B., B.R.S. ; writing –review & editing, A.K.B., J.Z., C.Y., G.C., E.I., A.L.C., C.M.H., J.K.K., W.C.P., B.R.S.; visualization, A.K.B., B.R.S.; supervision, A.K.B., J.Z., C.Y., G.C., W.C.P., B.R.S.; funding acquisition, B.R.S

Declaration of interests:

No competing interests.

References:

Abood, R.N., McHugh, K.J., Rich, H.E., Ortiz, M.A., Tobin, J.M., Ramanan, K., Robinson, K.M., Bomberger, J.M., Kolls, J.K., Manni, M.L.*, et al.* (2019). IL-22-binding protein exacerbates influenza, bacterial super-infection. Mucosal Immunol *12*, 1231-1243.

Ahlfors, H., Morrison, P.J., Duarte, J.H., Li, Y., Biro, J., Tolaini, M., Di Meglio, P., Potocnik, A.J., and Stockinger, B. (2014). IL-22 fate reporter reveals origin and control of IL-22 production in homeostasis and infection. J Immunol *193*, 4602-4613.

Aparicio-Domingo, P., Romera-Hernandez, M., Karrich, J.J., Cornelissen, F., Papazian, N., Lindenbergh-Kortleve, D.J., Butler, J.A., Boon, L., Coles, M.C., Samsom, J.N.*, et al.* (2015). Type 3 innate lymphoid cells maintain intestinal epithelial stem cells after tissue damage. J Exp Med *212*, 1783-1791.

Aran, D., Looney, A.P., Liu, L., Wu, E., Fong, V., Hsu, A., Chak, S., Naikawadi, R.P., Wolters, P.J., Abate, A.R.*, et al.* (2019). Reference-based analysis of lung single-cell sequencing reveals a transitional profibrotic macrophage. Nat Immunol *20*, 163-172.

Ashburner, M., Ball, C.A., Blake, J.A., Botstein, D., Butler, H., Cherry, J.M., Davis, A.P., Dolinski, K., Dwight, S.S., Eppig, J.T.*, et al.* (2000). Gene ontology: tool for the unification of biology. The Gene Ontology Consortium. Nat Genet *25*, 25-29.

Barrow, A.D., Edeling, M.A., Trifonov, V., Luo, J., Goyal, P., Bohl, B., Bando, J.K., Kim, A.H., Walker, J., Andahazy, M.*, et al.* (2018). Natural Killer Cells Control Tumor Growth by Sensing a Growth Factor. Cell *172*, 534-548 e519.

Blanpain, C., and Fuchs, E. (2014). Stem cell plasticity. Plasticity of epithelial stem cells in tissue regeneration. Science *344*, 1242281.

Boniface, K., Bernard, F.X., Garcia, M., Gurney, A.L., Lecron, J.C., and Morel, F. (2005). IL-22 inhibits epidermal differentiation and induces proinflammatory gene expression and migration of human keratinocytes. J Immunol *174*, 3695-3702.

Butler, A., Hoffman, P., Smibert, P., Papalexi, E., and Satija, R. (2018). Integrating single-cell transcriptomic data across different conditions, technologies, and species. Nat Biotechnol *36*, 411-420.

Carraro, G., Mulay, A., Yao, C., Mizuno, T., Konda, B., Petrov, M., Lafkas, D., Arron, J.R., Hogaboam, C.M., Chen, P.*, et al.* (2020). Single-Cell Reconstruction of Human Basal Cell Diversity in Normal and Idiopathic Pulmonary Fibrosis Lungs. Am J Respir Crit Care Med *202*, 1540-1550.

Davis, J.D., and Wypych, T.P. (2021). Cellular and functional heterogeneity of the airway epithelium. Mucosal Immunol.

Edgar, R., Domrachev, M., and Lash, A. (2002). Gene Expression Omnibus: NCBI gene expression and hybridization array data repository. Nucleic Acids Res.

Fang, Y., Liu, H., Huang, H., Li, H., Saqi, A., Qiang, L., and Que, J. (2020). Distinct stem/progenitor cells proliferate to regenerate the trachea, intrapulmonary airways and alveoli in COVID-19 patients. Cell Res *30*, 705-707.

Fernanda de Mello Costa, M., Weiner, A.I., and Vaughan, A.E. (2020). Basal-like Progenitor Cells: A Review of Dysplastic Alveolar Regeneration and Remodeling in Lung Repair. Stem Cell Reports *15*, 1015-1025.

Gene Ontology, C. (2021). The Gene Ontology resource: enriching a GOld mine. Nucleic Acids Res *49*, D325-D334.

Haas, M., Gomez Vazquez, J.L., Sun, D.I., Tran, H.T., Brislinger, M., Tasca, A., Shomroni, O., Vleminckx, K., and Walentek, P. (2019). DeltaN-Tp63 Mediates Wnt/beta-Catenin-Induced Inhibition of Differentiation in Basal Stem Cells of Mucociliary Epithelia. Cell Rep *28*, 3338-3352 e3336.

Hackett, T.L., Singhera, G.K., Shaheen, F., Hayden, P., Jackson, G.R., Hegele, R.G., Van Eeden, S., Bai, T.R., Dorscheid, D.R., and Knight, D.A. (2011). Intrinsic phenotypic differences of asthmatic epithelium and its inflammatory responses to respiratory syncytial virus and air pollution. Am J Respir Cell Mol Biol *45*, 1090-1100.

Harfe, B.D., Scherz, P.J., Nissim, S., Tian, H., McMahon, A.P., and Tabin, C.J. (2004). Evidence for an expansion-based temporal Shh gradient in specifying vertebrate digit identities. Cell *118*, 517-528.

Hebert, K.D., McLaughlin, N., Galeas-Pena, M., Zhang, Z., Eddens, T., Govero, A., Pilewski, J.M., Kolls, J.K., and Pociask, D.A. (2020). Targeting the IL-22/IL-22BP axis enhances tight junctions and reduces inflammation during influenza infection. Mucosal Immunol *13*, 64-74.
Hogan, B.L., Barkauskas, C.E., Chapman, H.A., Epstein, J.A., Jain, R., Hsia, C.C., Niklason, L., Calle, E., Le, A., Randell, S.H.*, et al.* (2014). Repair and regeneration of the respiratory system: complexity, plasticity, and mechanisms of lung stem cell function. Cell Stem Cell *15*, 123-138.
Iacono, G., Massoni-Badosa, R., and Heyn, H. (2019). Single-cell transcriptomics unveils gene regulatory network plasticity. Genome Biol *20*, 110.
Iacono, G., Mereu, E., Guillaumet-Adkins, A., Corominas, R., Cusco, I., Rodriguez-Esteban, G., Gut, M., Perez-Jurado, L.A., Gut, I., and Heyn, H. (2018). bigSCale: an analytical framework for big-scale single-cell data. Genome Res *28*, 878-890.
Jin, C., Lagoudas, G.K., Zhao, C., Bullman, S., Bhutkar, A., Hu, B., Ameh, S., Sandel, D., Liang, X.S., Mazzilli, S.*, et al.* (2019). Commensal Microbiota Promote Lung Cancer Development via gammadelta T Cells. Cell *176*, 998-1013 e1016.
Katsura, H., Kobayashi, Y., Tata, P.R., and Hogan, B.L.M. (2019). IL-1 and TNFalpha Contribute to the Inflammatory Niche to Enhance Alveolar Regeneration. Stem Cell Reports *12*, 657-666.
Kempski, J., Brockmann, L., Gagliani, N., and Huber, S. (2017). TH17 Cell and Epithelial Cell Crosstalk during Inflammatory Bowel Disease and Carcinogenesis. Front Immunol *8*, 1373.
Korotkevich, G., Sukhov, V., Budin, N., Shpak, B., Artyomov, M.N., and Sergushichev, A. (2021).
Kumar, P.A., Hu, Y., Yamamoto, Y., Hoe, N.B., Wei, T.S., Mu, D., Sun, Y., Joo, L.S., Dagher, R., Zielonka, E.M.*, et al.* (2011). Distal airway stem cells yield alveoli in vitro and during lung regeneration following H1N1 influenza infection. Cell *147*, 525-538.
La Manno, G., Soldatov, R., Zeisel, A., Braun, E., Hochgerner, H., Petukhov, V., Lidschreiber, K., Kastriti, M.E., Lonnerberg, P., Furlan, A.*, et al.* (2018). RNA velocity of single cells. Nature *560*, 494-498.
Liberzon, A., Birger, C., Thorvaldsdottir, H., Ghandi, M., Mesirov, J.P., and Tamayo, P. (2015). The Molecular Signatures Database (MSigDB) hallmark gene set collection. Cell Syst *1*, 417-425.
Lindemans, C.A., Calafiore, M., Mertelsmann, A.M., O'Connor, M.H., Dudakov, J.A., Jenq, R.R., Velardi, E., Young, L.F., Smith, O.M., Lawrence, G.*, et al.* (2015). Interleukin-22 promotes intestinal-stem-cell-mediated epithelial regeneration. Nature *528*, 560-564.
Lo, B.C., Shin, S.B., Canals Hernaez, D., Refaeli, I., Yu, H.B., Goebeler, V., Cait, A., Mohn, W.W., Vallance, B.A., and McNagny, K.M. (2019). IL-22 Preserves Gut Epithelial Integrity and Promotes Disease Remission during Chronic Salmonella Infection. J Immunol *202*, 956-965.
Madisen, L., Zwingman, T.A., Sunkin, S.M., Oh, S.W., Zariwala, H.A., Gu, H., Ng, L.L., Palmiter, R.D., Hawrylycz, M.J., Jones, A.R.*, et al.* (2010). A robust and high-throughput Cre reporting and characterization system for the whole mouse brain. Nat Neurosci *13*, 133-140.
McGee, H.M., Schmidt, B.A., Booth, C.J., Yancopoulos, G.D., Valenzuela, D.M., Murphy, A.J., Stevens, S., Flavell, R.A., and Horsley, V. (2013). IL-22 promotes fibroblast-mediated wound repair in the skin. J Invest Dermatol *133*, 1321-1329.
Mi, H., Muruganujan, A., Casagrande, J.T., and Thomas, P.D. (2013). Large-scale gene function analysis with the PANTHER classification system. Nat Protoc *8*, 1551-1566.
Muzumdar, M.D., Tasic, B., Miyamichi, K., Li, L., and Luo, L. (2007). A global double-fluorescent Cre reporter mouse. Genesis *45*, 593-605.
Plummer, N.W., Evsyukova, I.Y., Robertson, S.D., de Marchena, J., Tucker, C.J., and Jensen, P. (2015). Expanding the power of recombinase-based labeling to uncover cellular diversity. Development *142*, 4385-4393.
Pociask, D.A., Scheller, E.V., Mandalapu, S., McHugh, K.J., Enelow, R.I., Fattman, C.L., Kolls, J.K., and Alcorn, J.F. (2013). IL-22 is essential for lung epithelial repair following influenza infection. Am J Pathol *182*, 1286-1296.
Rackley, C.R., and Stripp, B.R. (2012). Building and maintaining the epithelium of the lung. J Clin Invest *122*, 2724-2730.

Rawlins, E.L., Okubo, T., Xue, Y., Brass, D.M., Auten, R.L., Hasegawa, H., Wang, F., and Hogan, B.L. (2009). The role of Scgb1a1+ Clara cells in the long-term maintenance and repair of lung airway, but not alveolar, epithelium. Cell Stem Cell *4*, 525-534.
Ray, S., Chiba, N., Yao, C., Guan, X., McConnell, A.M., Brockway, B., Que, L., McQualter, J.L., and Stripp, B.R. (2016). Rare SOX2(+) Airway Progenitor Cells Generate KRT5(+) Cells that Repopulate Damaged Alveolar Parenchyma following Influenza Virus Infection. Stem Cell Reports *7*, 817-825.
Rock, J.R., Barkauskas, C.E., Cronce, M.J., Xue, Y., Harris, J.R., Liang, J., Noble, P.W., and Hogan, B.L. (2011). Multiple stromal populations contribute to pulmonary fibrosis without evidence for epithelial to mesenchymal transition. Proc Natl Acad Sci U S A *108*, E1475-1483.
Rock, J.R., Randell, S.H., and Hogan, B.L. (2010). Airway basal stem cells: a perspective on their roles in epithelial homeostasis and remodeling. Dis Model Mech *3*, 545-556.
Schindelin, J., Arganda-Carreras, I., Frise, E., Kaynig, V., Longair, M., Pietzsch, T., Preibisch, S., Rueden, C., Saalfeld, S., Schmid, B.*, et al.* (2012). Fiji: an open-source platform for biological-image analysis. Nat Methods *9*, 676-682.
Seibold, M.A., Smith, R.W., Urbanek, C., Groshong, S.D., Cosgrove, G.P., Brown, K.K., Schwarz, M.I., Schwartz, D.A., and Reynolds, S.D. (2013). The idiopathic pulmonary fibrosis honeycomb cyst contains a mucocilary pseudostratified epithelium. PloS one *8*, e58658.
Stuart, T., Butler, A., Hoffman, P., Hafemeister, C., Papalexi, E., Mauck, W.M., 3rd, Hao, Y., Stoeckius, M., Smibert, P., and Satija, R. (2019). Comprehensive Integration of Single-Cell Data. Cell *177*, 1888-1902 e1821.
Subramanian, A., Tamayo, P., Mootha, V.K., Mukherjee, S., Ebert, B.L., Gillette, M.A., Paulovich, A., Pomeroy, S.L., Golub, T.R., Lander, E.S.*, et al.* (2005). Gene set enrichment analysis: a knowledge-based approach for interpreting genome-wide expression profiles. Proc Natl Acad Sci U S A *102*, 15545-15550.
Tata, A., Kobayashi, Y., Chow, R.D., Tran, J., Desai, A., Massri, A.J., McCord, T.J., Gunn, M.D., and Tata, P.R. (2018). Myoepithelial Cells of Submucosal Glands Can Function as Reserve Stem Cells to Regenerate Airways after Injury. Cell Stem Cell *22*, 668-683 e666.
Tata, P.R., Mou, H., Pardo-Saganta, A., Zhao, R., Prabhu, M., Law, B.M., Vinarsky, V., Cho, J.L., Breton, S., Sahay, A.*, et al.* (2013). Dedifferentiation of committed epithelial cells into stem cells in vivo. Nature *503*, 218-223.
Tata, P.R., and Rajagopal, J. (2017). Plasticity in the lung: making and breaking cell identity. Development *144*, 755-766.
Tavares, L.P., Teixeira, M.M., and Garcia, C.C. (2017). The inflammatory response triggered by Influenza virus: a two edged sword. Inflamm Res *66*, 283-302.
Van Keymeulen, A., Rocha, A.S., Ousset, M., Beck, B., Bouvencourt, G., Rock, J., Sharma, N., Dekoninck, S., and Blanpain, C. (2011). Distinct stem cells contribute to mammary gland development and maintenance. Nature *479*, 189-193.
Vaughan, A.E., Brumwell, A.N., Xi, Y., Gotts, J.E., Brownfield, D.G., Treutlein, B., Tan, K., Tan, V., Liu, F.C., Looney, M.R.*, et al.* (2015). Lineage-negative progenitors mobilize to regenerate lung epithelium after major injury. Nature *517*, 621-625.
Xi, Y., Kim, T., Brumwell, A.N., Driver, I.H., Wei, Y., Tan, V., Jackson, J.R., Xu, J., Lee, D.K., Gotts, J.E.*, et al.* (2017). Local lung hypoxia determines epithelial fate decisions during alveolar regeneration. Nat Cell Biol *19*, 904-914.
Xu, Y., Mizuno, T., Sridharan, A., Du, Y., Guo, M., Tang, J., Wikenheiser-Brokamp, K.A., Perl, A.T., Funari, V.A., Gokey, J.J.*, et al.* (2016). Single-cell RNA sequencing identifies diverse roles of epithelial cells in idiopathic pulmonary fibrosis. JCI Insight *1*, e90558.
Yang, Y., Riccio, P., Schotsaert, M., Mori, M., Lu, J., Lee, D.K., Garcia-Sastre, A., Xu, J., and Cardoso, W.V. (2018). Spatial-Temporal Lineage Restrictions of Embryonic p63(+) Progenitors Establish Distinct Stem Cell Pools in Adult Airways. Dev Cell *44*, 752-761 e754.
Zheng, M., Horne, W., McAleer, J.P., Pociask, D., Eddens, T., Good, M., Gao, B., and Kolls, J.K. (2016). Therapeutic Role of Interleukin 22 in Experimental Intra-abdominal Klebsiella pneumoniae Infection in Mice. Infect Immun *84*, 782-789.

Zheng, Y., Valdez, P.A., Danilenko, D.M., Hu, Y., Sa, S.M., Gong, Q., Abbas, A.R., Modrusan, Z., Ghilardi, N., de Sauvage, F.J., *et al.* (2008). Interleukin-22 mediates early host defense against attaching and effacing bacterial pathogens. Nat Med *14*, 282-289.
Zuo, W., Zhang, T., Wu, D.Z., Guan, S.P., Liew, A.A., Yamamoto, Y., Wang, X., Lim, S.J., Vincent, M., Lessard, M., *et al.* (2015). p63(+)Krt5(+) distal airway stem cells are essential for lung regeneration. Nature *517*, 616-620.

Fig. 1 ScRNAseq to reveal the molecular phenotype of lung epithelial cells during the course of recovery following PR8 influenza virus infection.

(A) Experimental design. Mouse lung homogenates were collected from 8–12-week-old C57/Bl6 and *Sftpc-CreER*/*ROSA-mTmG* mice (n = 5 per group). Lung tissue was collected at indicated time points and either total epithelial cells (C57/Bl6 mice) or AT2 depleted epithelial cells (*Sftpc-CreER*/*ROSA-mTmG* mice) enriched by FACS.

(B) UMAP plot of combined scRNAseq data. Unsupervised clustering was used to distinguish distinct cell phenotypes which were assigned to known epithelial cell types based upon gene signatures. Pie chart shows fractional representation of each cell types within the entire data set.

(C) Heatmap showing unique molecular profiles between cell types. Top 3 genes for each cell category are annotated to the left. Full gene lists for each cell category are provided in Supp. Fig. 1A.

(D) Representation of serous (red bars) and basal (black bars) cell types as a function of percent total sampled cells at each recovery time point. dpi = days post infection.

(E) UMAP plot tracking relative changes in basal and serous cell populations for indicated samples. B-A = bronchioalveolar.

(F) Assessment of BC gene signature during recovery from PR8-induced injury. T-B = tracheal bronchial.

(G) Dot plot comparing expression of selected club and serous cell-specific genes between cell types.

(H) Representative immunofluorescence colocalization of either Msln or Bpifa1 (green) with Scgb3a2 (red) within conducting airway epithelium.

Fig. 2 Single cell and spatial gene expression profiling to investigate lineage relationships between serous and basal cells following PR8 infection.

(A) Comparative analysis of normalized enrichment for mitotic gene sets by cell type & condition. Red bars represent conditions with adjusted p value <0.05.

(B) Experimental design for generation of RNA velocity projections. Single cell RNAseq data were first subsetted by cell type (basal, serous, and club), followed by time following infection (early: naïve, 3, 5, 7, 9 and 11 dpi, or late: 14, 17, 21 and 240 dpi).

(C) Trajectory inference based upon RNA velocity profiling among basal, serous and club cell subsets.

(D) Experimental design for generation of spatial gene expression data.

(E) UMAP plot of Visium spot transcriptome clusters. Unsupervised hierarchical clustering revealed the presence of 7 transcriptionally distinct spot clusters.

(F) Heatmap showing the presence of unique molecular profiles between spot clusters defined in “E”.

(G) Projection of spot clusters onto H&E image of tissue sample.

(H) Cell type prediction scores of epithelial populations represented within spatial RNAseq data. Cell type specific gene signatures were generated using scRNAseq data in Fig. 1 A. Color scale at bottom reflects intensity of cell type prediction scores.

(I) Spatial gene expression of cell type-specific marker genes mapped onto spot coordinates from region sampled in red box in Fig. 2G: *Krt5* (basal), *Scgb3a2* (serous and club), *Scgb1a1* (club) and *Cldn10* (club) markers. Color scale at bottom reflects abundance of indicated transcripts.

(J) Scatter plot of data from spot cluster 5 (Fig. 2E), showing correlation coefficients of transcript levels for either *Scgb3a2* or *Scgb1a1*, with *Krt5*.

(K) Representative immunofluorescence colocalization of either Cldn10, Scgb1a1, or Scgb3a2 (red), with Krt5 (green), within injured distal airway of 14 dpi PR8 infected mice.

Fig. 3 Rare Scgb3a2^{+}/Scgb1a1^{-} serous cells reside within intralobar epithelium and assume BC fates in response to PR8-induced airway injury.

(A) Schematic illustration of recombinase driver and reporter alleles used in Dre/Cre recombinase (DR) mice for independent lineage labeling of serous and club cells.

(B) Experimental design. DR mice (n = 5 per experimental group) were treated with 3 doses of TM, infected with PR8 and recovered for the indicated time points.

(C) Representative immunofluorescence localization of tdT (Lin^{3a2}; red) and eGFP (Lin3$^{a2/1a1}$; green) lineage reporters reflective of serous and club cells, respectively. Shown is a low magnification image (left) and selected high magnification images of either proximal (i) or distal (ii) airway epithelium (right).

(D) Representative immunofluorescence colocalization of lineage reporters (green or red) with either Scgb3a2, Bpifa1, Foxj1, or Krt5 (white) in airways of naïve mice.

(E) Representative immunofluorescence colocalization of lineage reporters (green or red) with Krt5 (white) at indicated time points after PR8 infection.

(F) Representative immunofluorescence colocalization of lineage reporters (green or red) with Krt5 (white) 14 days after PR8 infection, demonstrating Lin^{3a2}high and -low epithelial cells.

(G) Representative immunofluorescence colocalization of tdT (Lin^{3a2}; red) with Krt5 (green) among lineage-positive alveolar clusters 21 days after PR8 infection.

(H) Schematic representation of serous to basal cell transitions occurring in airways and alveoli following PR8 infection.

(I) Quantification of recombination efficiency following immunofluorescent staining for tdT, eGFP and Scgb3a2 (as in “D”). Red bars show either Scgb3a2 or lineage traced (either tdT or eGFP) cells per unit basement membrane. Black bar represents the fractional representation of Scgb3a2-immunofluoresecnt cells that are lineage positive.

(J) Contribution of lineage-tagged populations to nascent BC in airways as a function of time after PR8 infection (G). N=3 per condition, with significance determined by Mann-Whitney U-test.
(K) Contribution of lineage-tagged populations to nascent BC in alveolar “pods” as a function of time after PR8 infection (G). N=3 per condition, with significance determined by Mann-Whitney U-test.

Fig. 4 Gene regulatory network analysis of PR8 infected BC reveal induction of Stat3 signaling during injury.

(A) Experimental design for generation of GRNs. ScRNAseq data were first subsetted by cell type followed by segregation into early vs late recovery time points, resulting in the creation of four networks for downstream analysis.
(B) Table showing node and edge number after homogenization of late time points to their respective naïve controls.
(C) Visualization of GRNs. Node and font sizes reflect degree centrality and strength of connectivity. The top five genes with the highest delta centrality value relative to naïve controls are highlighted in green, with remaining genes shown in red.
(D) Representation of significant GO terms associated with immune>epithelial interaction enriched among PR8-infected BC (upper) and IS cells (lower) using a Panther overrepresentation test.
(E) Assessment of selected cytokine levels in BALF during recovery from PR8 infection. 4-5 biological replicates were used per timepoint with statistical significance determined by Mann-Whitney U-test.

Fig. 5 T lymphoid cells colocalize with nascent BC at sites of lung injury following PR8 infection.

(A) Experimental design. Mouse lung homogenates were collected from 8-12-week-old C57/Bl6 mice, $CD45^{+}$ immune cells enriched by FACS and transcriptomes assessed by scRNAseq (n = 5 per group).
(B) UMAP plot of combined scRNAseq data. Unsupervised clustering was used to distinguish distinct cell phenotypes which were assigned to known immune cell types based upon gene signatures. Pie chart shows fractional representation of each cell types within the entire data set.
(C) Heatmap showing the presence of unique molecular profiles between T lymphoid, B lymphoid , and Myeloid subsets. Top 5 genes for each cell category are annotated to the left.
(D) Representation of major immune cell subsets as a function of total immune cells for each recovery time point.
(E) Dot plot showing expression of selected genes that reflect T-lymphoid subsets.
(F) Representation T-lymphoid subsets as a function of percent total sampled immune cells at each recovery time point.

(G) Cell type prediction scores of immune populations represented within spatial RNAseq data. Cell type specific gene signatures were generated using scRNAseq data in Fig. 5A. Color scale at bottom reflects intensity of cell type prediction scores.

(H) Cell type-specific marker genes mapped onto spot coordinates demonstrating co-localization of Krt5 and CD3g expression.

(I) Gene scatter plot showing co-expression of T Lymphoid (*CD3g, CD3e, CD3d*), Myeloid (*Lyz2, Mrc1, Itgam*), and B Lymphoid (*CD79a, CD79b, CD19*) markers with the BC marker Krt5 within spot clusters.

(J) UMAP plot of subsetted γδT cells. γδT cells were divided into type 17 and non-type 17 subsets using a type 17 gene signature (Supp. Fig. 4B).

(K) Stacked bar plot showing dynamic changes in type 17 γδT cells and non-type 17 γδT cells.

Fig. 6 Identity of IL-22 expressing cells and their localization to regions of BC hyperplasia in lungs of PR8 infected mice.

(A) Experimental design for fate mapping of IL-22 expressing cells following PR8 infection using *IL-22^{Cre}/ROSA-tdT* mice.

(B) Flow cytometry analysis of either BAL or tissue homogenate from PR8-infected *IL-22^{Cre}/ROSA-tdT* mice. IL22 lineage reporter (tdT; Lin^{+}) was assessed as a function of surface expression of CD3 and CD4 and data presented as the fraction of positive cells.

(C) Immunofluorescence detection of Lin^{+} cells as a function of p63-immunoreactive BC within BC-rich vs BC devoid alveolar epithelium of PR8-infected mice.

(D) Immunofluorescence localization of IL-22 expressing cells 7 and 14 days post-PR8 infection.

(E) Immunofluorescence colocalization of IL-22ra1 (red) with either a-tub (ciliated), Scgb3a2 (serous/club), Krt5 (BC), Scgb1a1 (club) (green) in airways of naïve mice.

(F) Representative immunofluorescent colocalization of IL-22ra1 (red) and Krt5 (green) in BC-rich alveolar region of PR8-infected mouse lung.

Fig. 7. IL-22 regulates BC fate in the PR8-injured lung.

(A) Experimental design to assess BC expansion in *IL-22^{Cre}* homozygous (IL-22-LOF) mice. Left lobes were collected for immunostaining and total RNA isolated from the right cranial lobe for gene expression analysis.

(B) Representative immunofluorescence localization of Pdpn (red) and Krt5 (green) in lungs of WT and IL-22-LOF mice 14 days post-PR8 infection.

(C) Quantification of (B). The fraction of Krt5 stained area was normalized to the area of damaged alveolar epithelium (DAPI^{+}Pdpn^{-}) (n = 3-5 biological replicates per group). Statistical analysis was performed by Mann-Whitney U-test.

(D) qPCR detection of *Krt5* mRNA in total lung RNA of PR8-infected WT and IL-22-LOF mice. 3-5 biological replicates were used per condition. Statistical analysis was performed by Mann-Whitney U-test.

(E) Representative immunofluorescence localization of Ki67 (red) and Krt5 (green) in lung tissue of PR8-infected WT, IL-22-LOF and *IL-22ra1*$^{fl/fl}$/*Shh-Cre* mice.

(F) Quantification of (E). Shown is the Ki67-labeling index for BC, expressed as percentage of Ki67^{+}, Krt5^{+} cells within areas of BC hyperplasia (n = 3-5 biological replicates per group). Statistical analysis was performed by Mann-Whitney U-test.

(G) Representative immunofluorescence localization of Krt5 (green) and Scgb3a2 (red) in lungs of PR8-infected WT, IL-22-LOF and *IL-22ra1*$^{fl/fl}$/*Shh-Cre* mice.

(H) Experimental design for scRNAseq of PR8-infected *IL-22ra1*$^{fl/fl}$/*Shh-Cre* mice (n = 5 biological replicates per group).

(I) UMAP plot of Sca1^{+} epithelial cells from IL-22ra1$^{fl/fl}$/*Shh-Cre* and C57/Bl6 control. Cell type annotation of clusters was performed based upon expression of cell type-specific genes.

(J) UMAP plot re-clustered based on genetic permutation to better represent changes in BC populations between experimental conditions.

(K) Assessment of *Krt5* and *Trp63* gene expression between IL-22ra1$^{fl/fl}$/*Shh-Cre* and WT control.

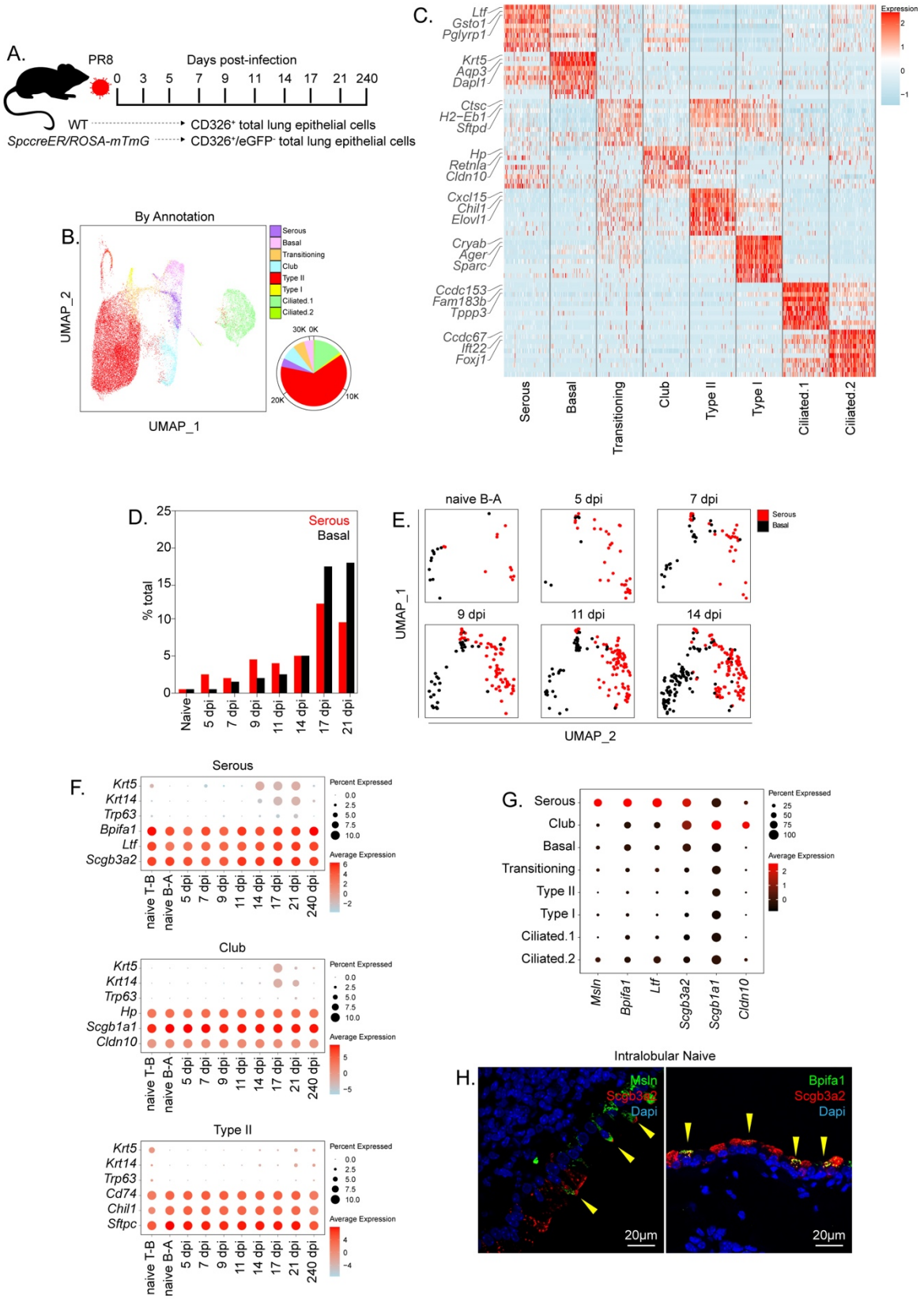

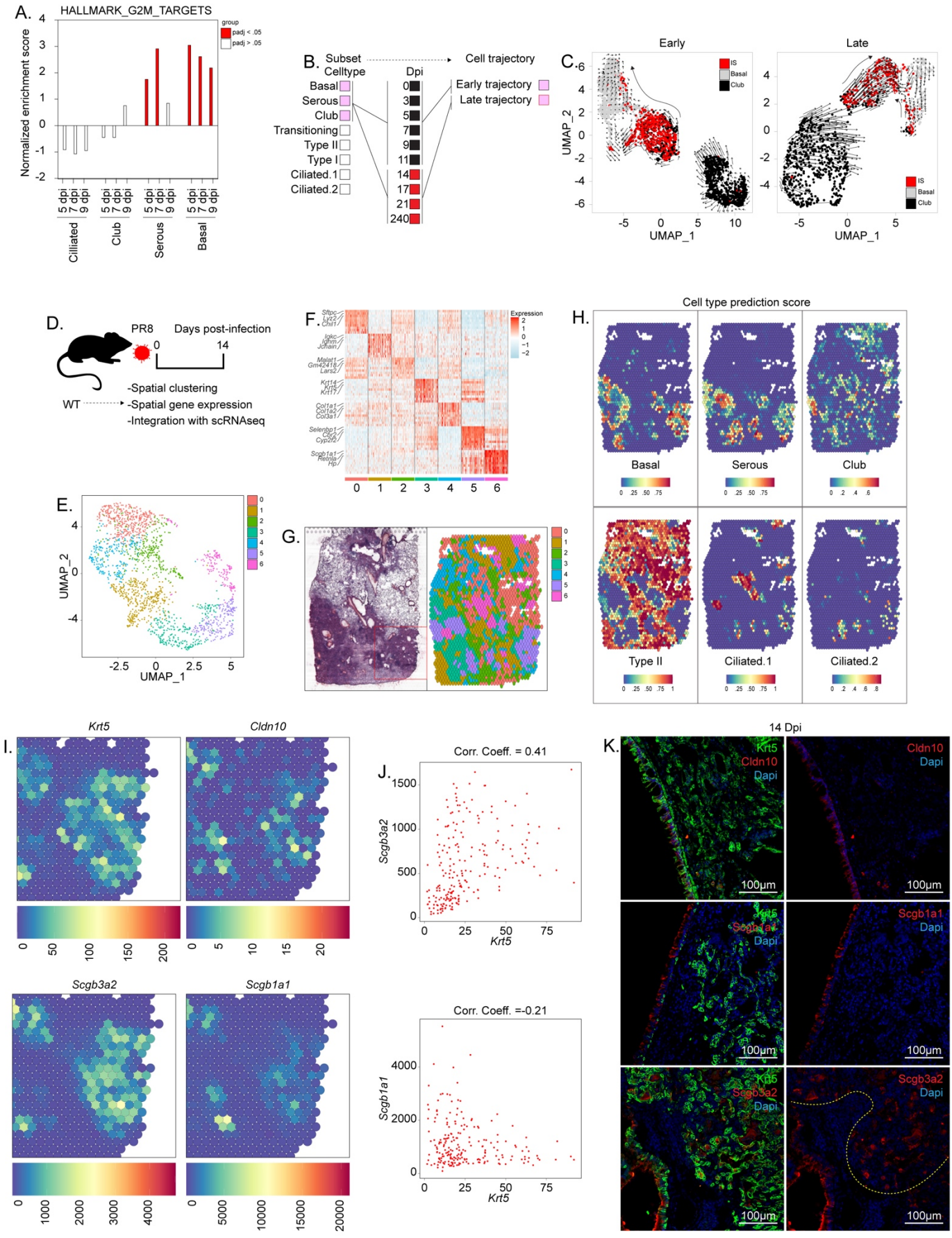

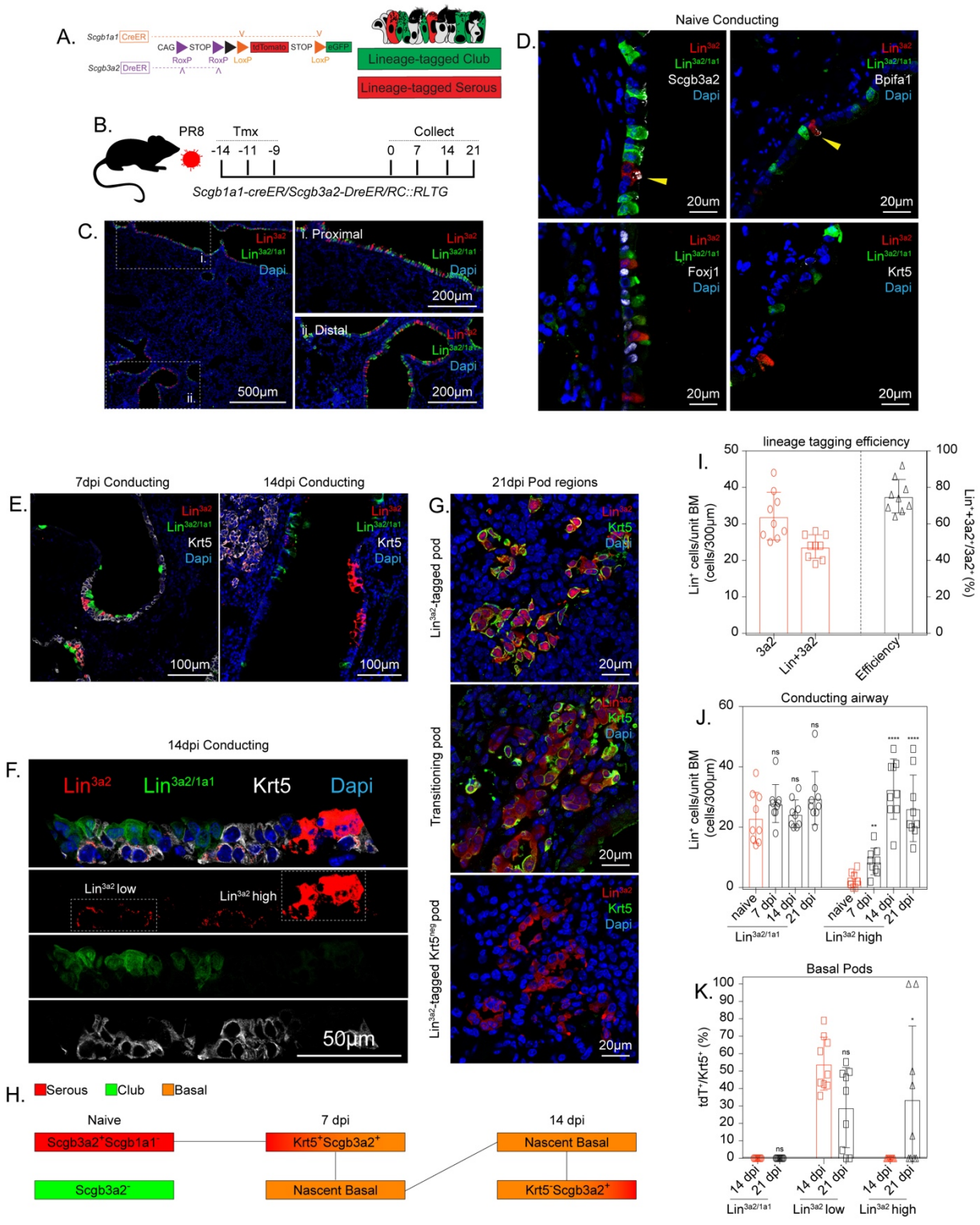

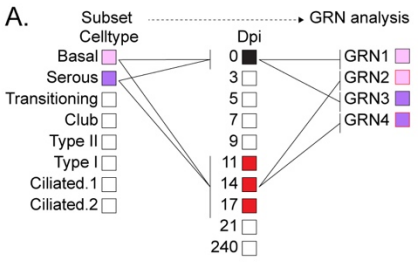

B.

	Nodes	Edges
GRN1: Naive_Basal	3886	7632
GRN2: Late_Basal	3233	7800
GRN3: Naive_Serous	5017	14624
GRN4: Late_Basal	4642	14505

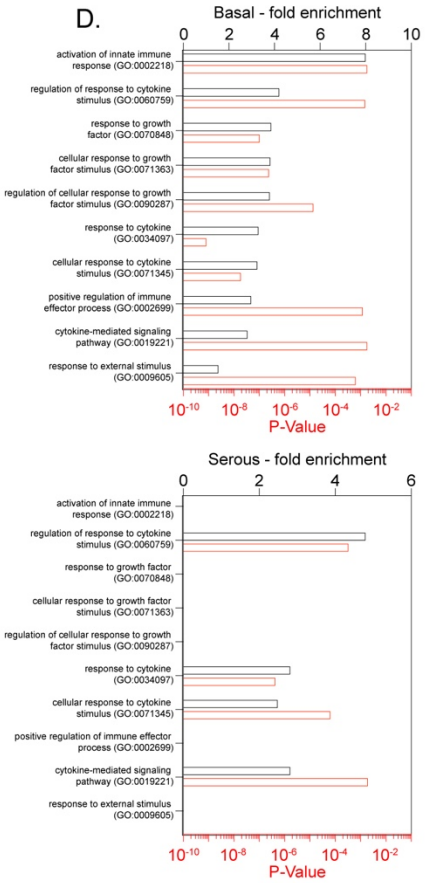

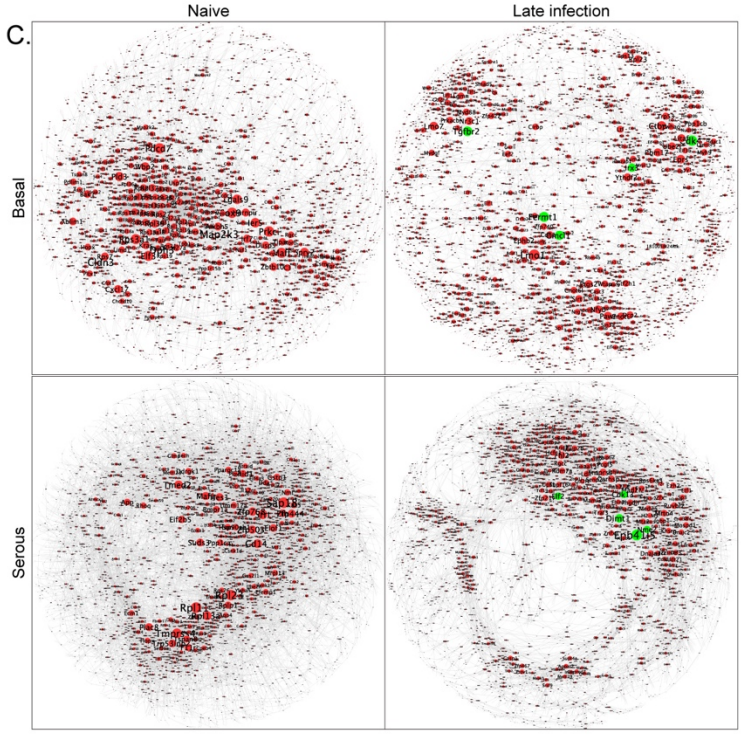

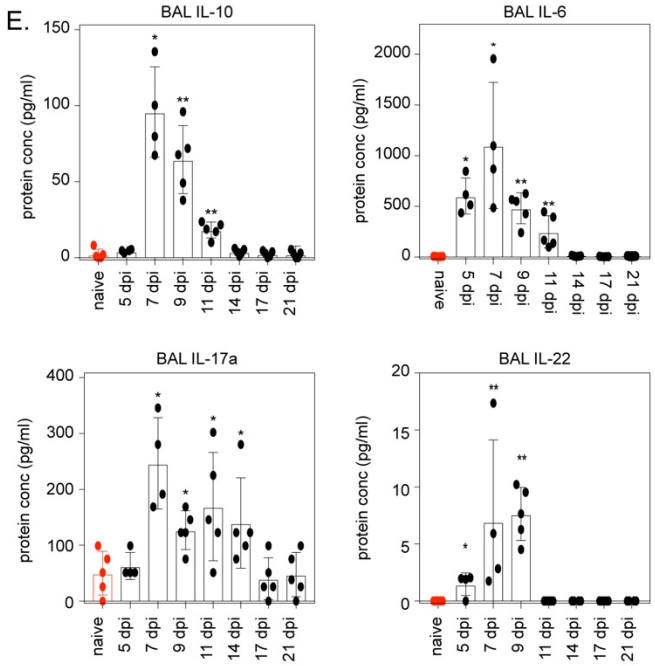

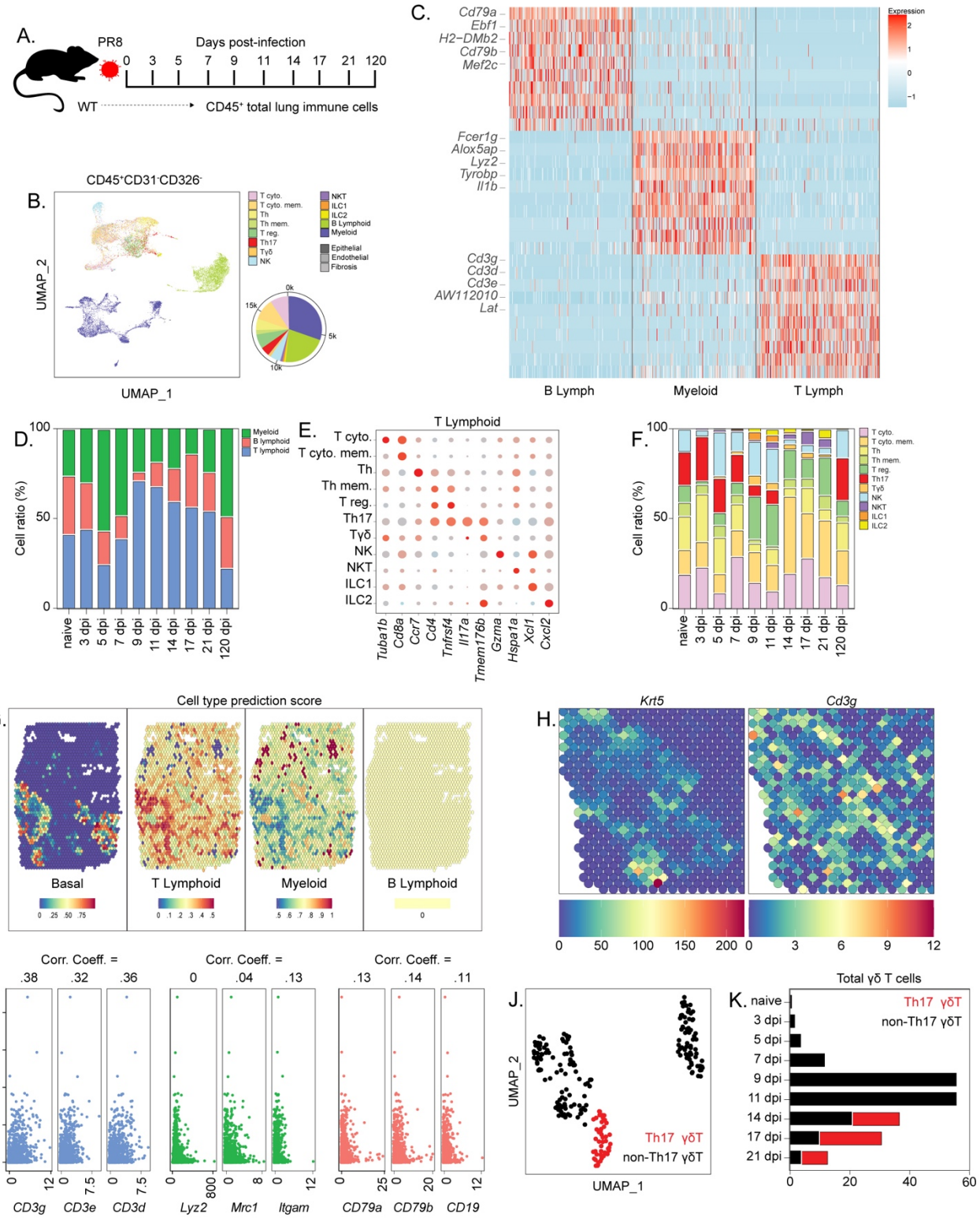

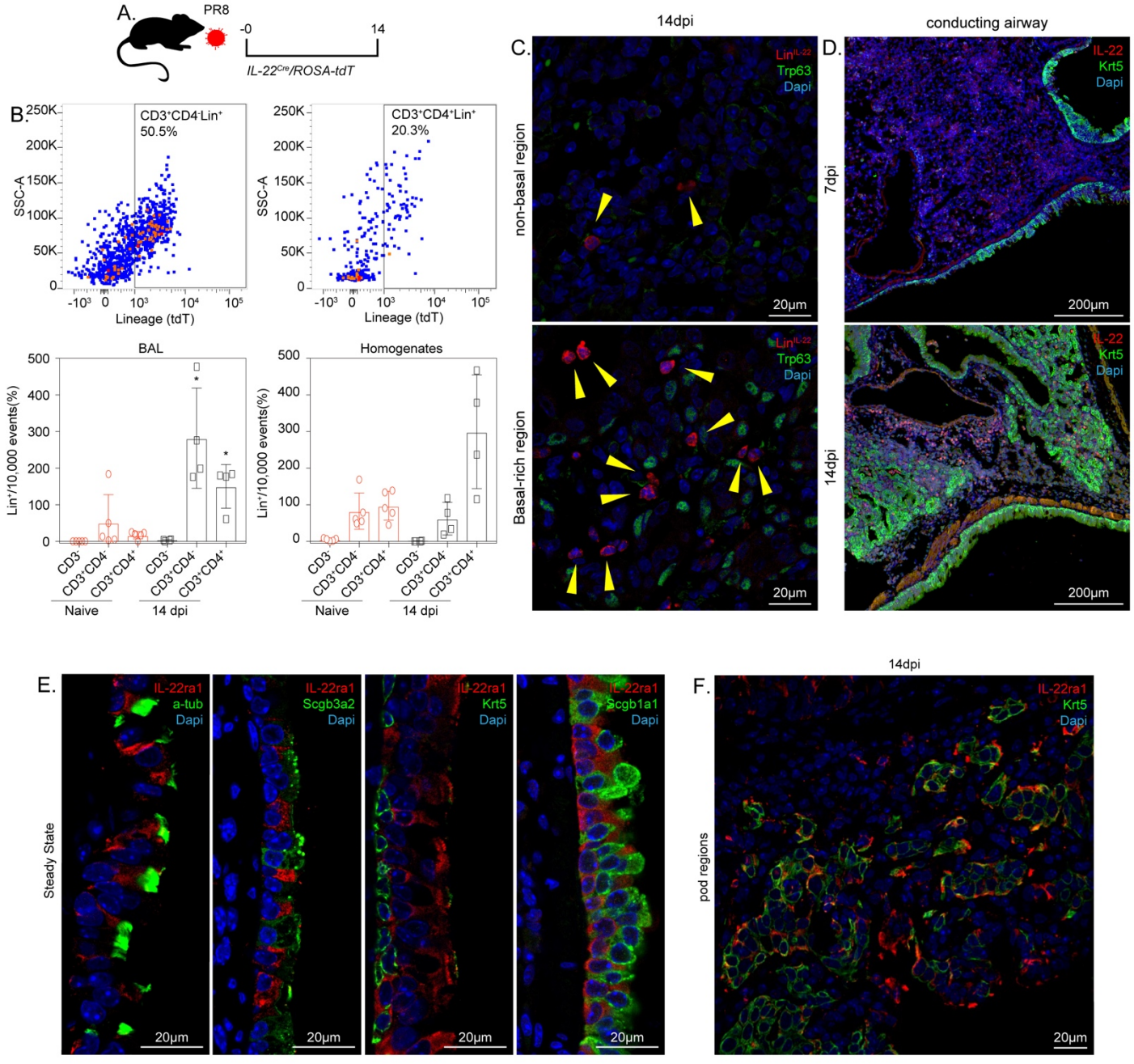

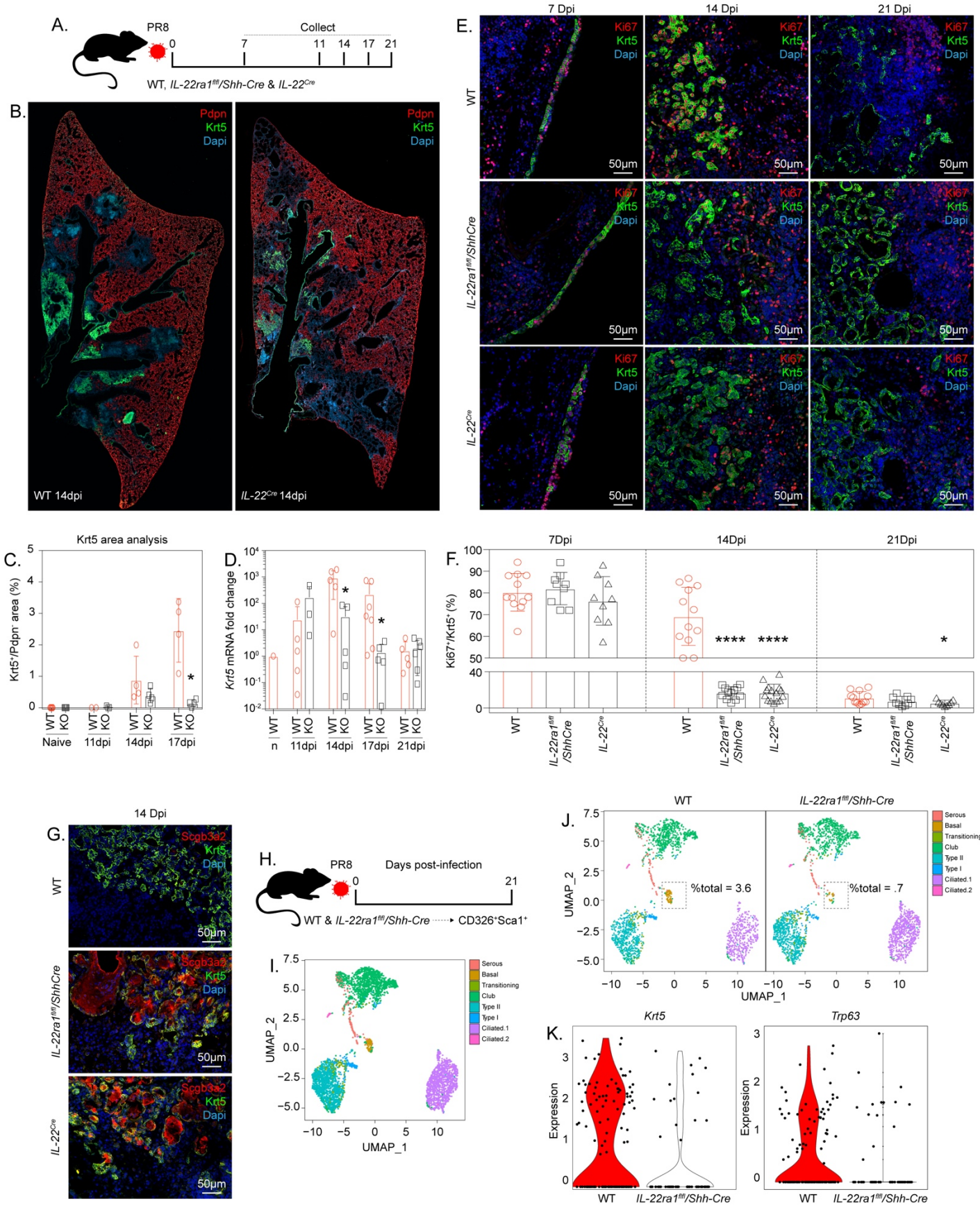

Supplemental Fig. 1. Club and IS cell cluster independently of cell cycle genes.

(A) Full gene list for heatmap shown in Fig 1. A.

(B) Violin plot comparing expression of selected antimicrobial genes at indicated time points after PR8 infection.

(C) Total G1_G2_G2M ratio between subsetted club and serous cells.

(D) Percent G1_G2_G2M ratio between subsetted club and serous cells.

(E) Principal component analysis between club and serous cells pre- & post-regression of cell cycle genes. Upper plots show points labeled by cell annotation and lower plots show points labeled according to G1_G2_G2M score.

Supplemental Fig. 2. Assessment of transcriptional differences between club and IS populations.

(A) Feature plot comparing expression of selected club and serous cell-specific genes between cell types.

Supplemental Fig. 3. Further characterization of DR mice in the context of influenza induced lung injury

(A) Representative immunofluorescence Single color images of Fig 3E. of lineage reporters (green or red) with Krt5 (white) at indicated time points after PR8 infection.

(B) Representative immunofluorescence colocalization of tdT (Lin^{3a2}; red) with Krt5 (green) & Scgb3a2 (white) among lineage-positive alveolar clusters 21 days after PR8 infection.

Supplemental Fig. 4. Temporal dynamics of cytokine expression during PR8 lung injury & characterization of transcriptional profile for type-17 γδT cells

(A) Assessment of cytokine levels in BALF & lung homogenate during recovery from PR8 infection. 4-5 biological replicates were used per timepoint with statistical significance determined by Mann-Whitney U-test.

(B) Feature plots showing expression of selected genes used to generate a signature for type-17 γδT cells.

(C) Stacked bar plot showing dynamic changes in Th17 T cells and non-Th17 T helper cells

Supplemental Fig. 5. Gating strategy for quantification of IL-22 expressing subsets using flow cytometry.

(A)Gating strategy to assess different IL-22 expressing cell types via flow cytometry. Cells were subsetted into $CD3^{-}Lin^{+}$, $CD3^{+}CD4^{-}Lin^{+}$ and $CD3^{+}CD4^{+}Lin^{+}$ populations to delineate non-T lymphoid, γδT and Th17 cells respectively.

Supplemental Fig. 6. Visualization of IL-22ra1 positive and negative BC regions during repair.

(A) Representative immunofluorescent colocalization of IL-22ra1 (red) and Krt5 (green) in BC-rich alveolar region of PR8-infected mouse lung.

Supplemental Fig. 7. Additional phenotyping for IL-22 LOF & *IL-22ra1$^{fl/fl}$/Shh-Cre*

(A) qPCR detection of viral gene mRNA in total lung RNA of PR8-infected WT, IL-22-LOF, and *IL-22ra1$^{fl/fl}$/Shh-Cre* mice. 3-5 biological replicates were used per condition. Statistical analysis was performed by Mann-Whitney U-test.

(B) Body weight changes of WT, IL-22-LOF, and *IL-22ra1$^{fl/fl}$/Shh-Cre* mice at different points during influenza induced acute lung injury.

(C) Representative immunofluorescence localization of Pdpn (red) and Krt5 (green) in lungs of *IL-22ra1$^{fl/fl}$/Shh-Cre* mice 14 days post-PR8 infection.

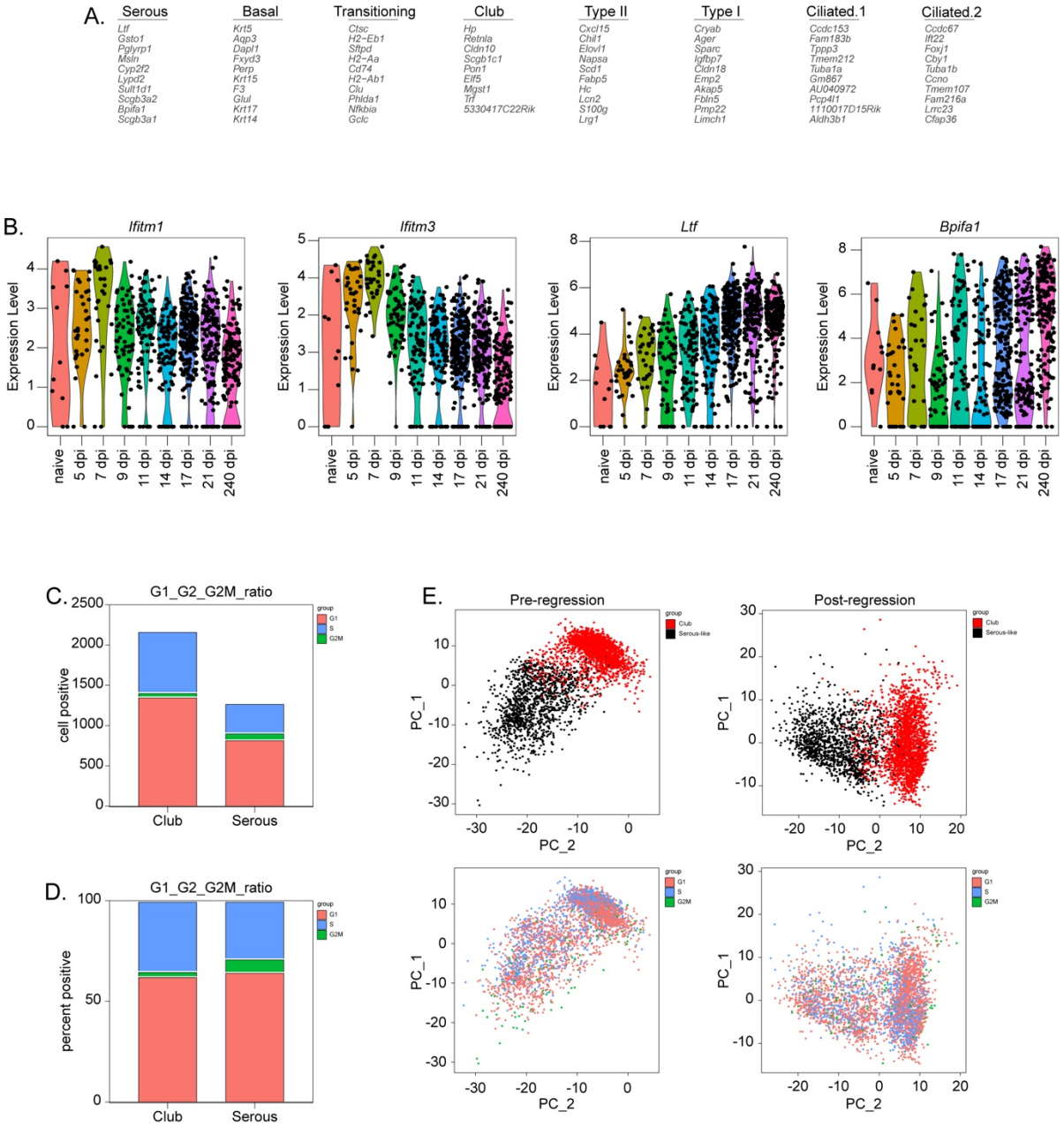

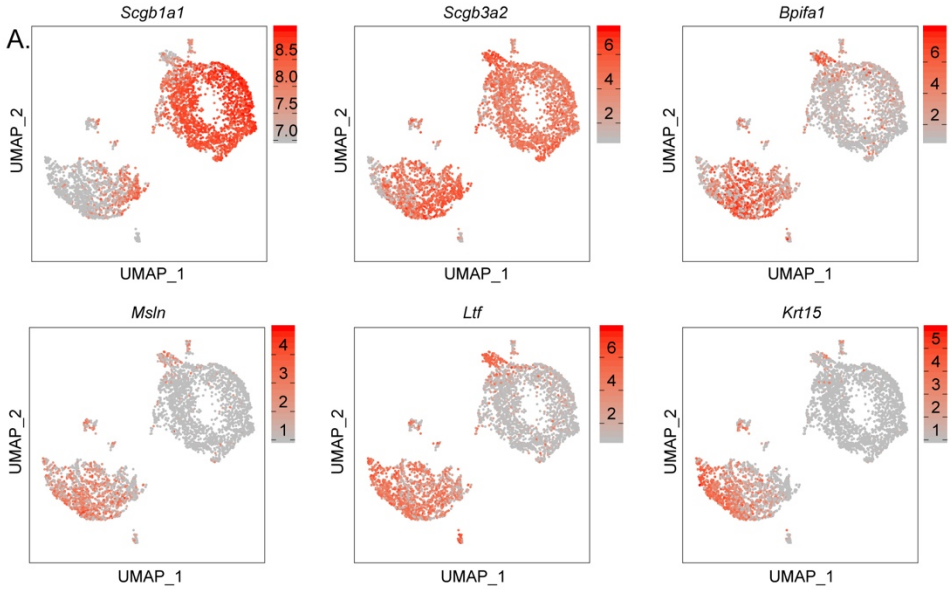

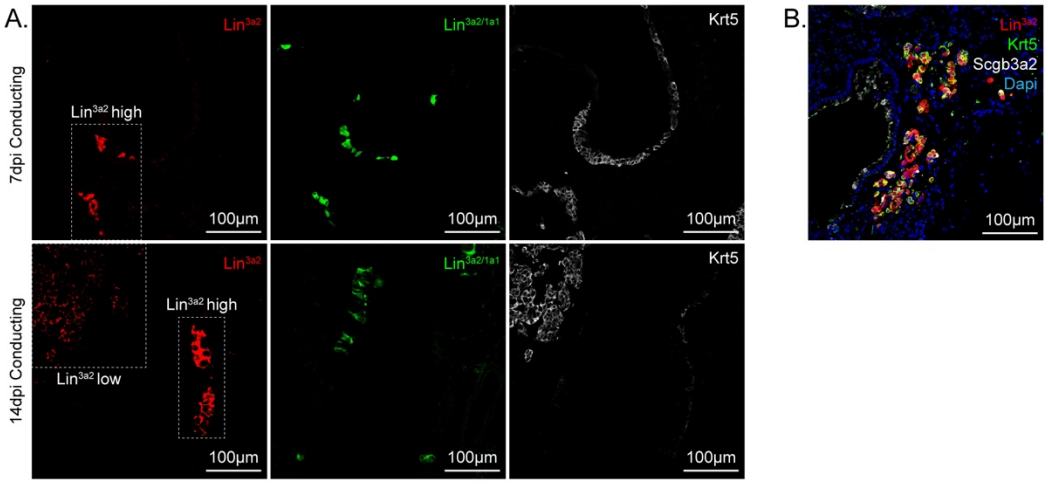

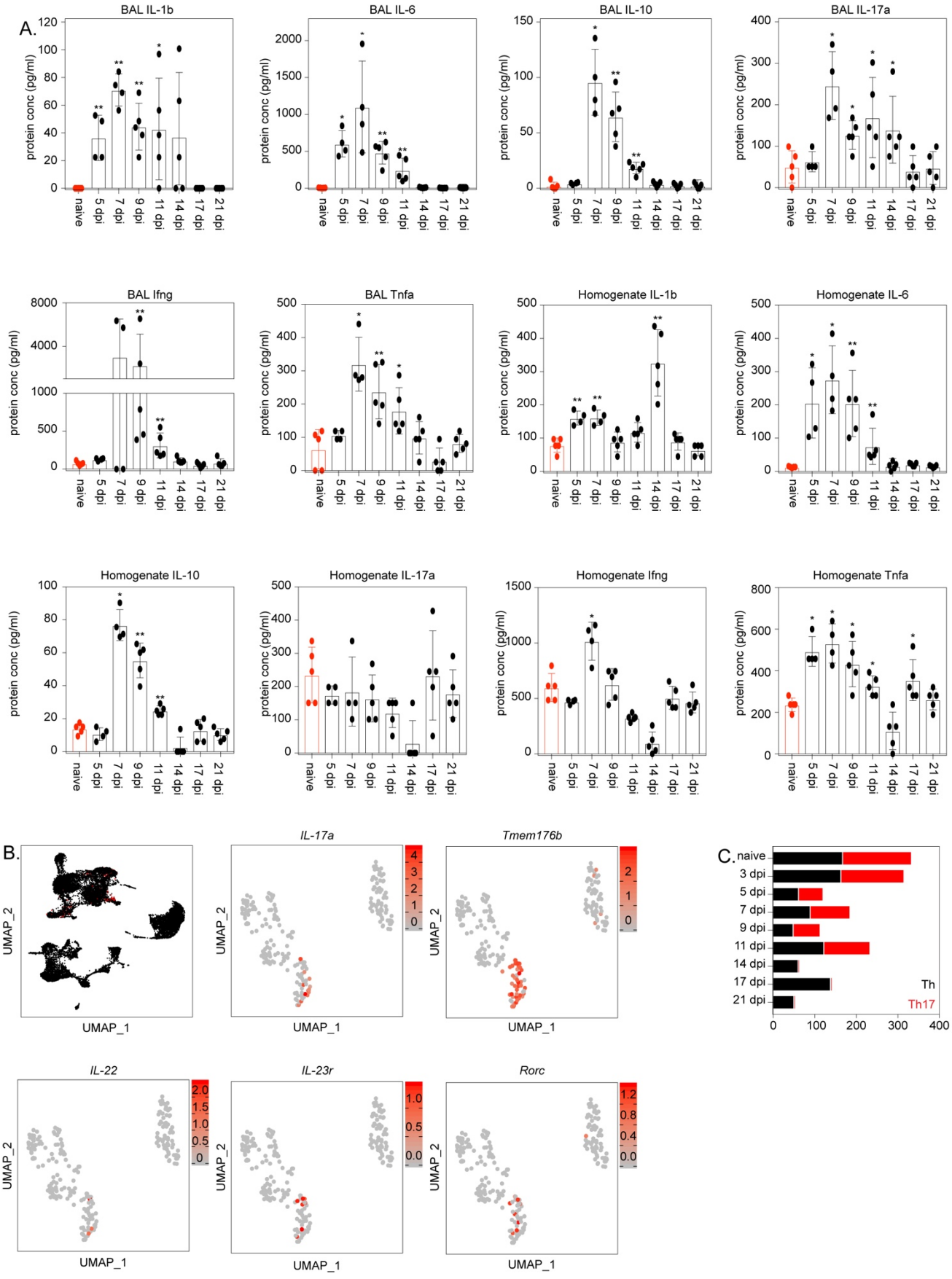

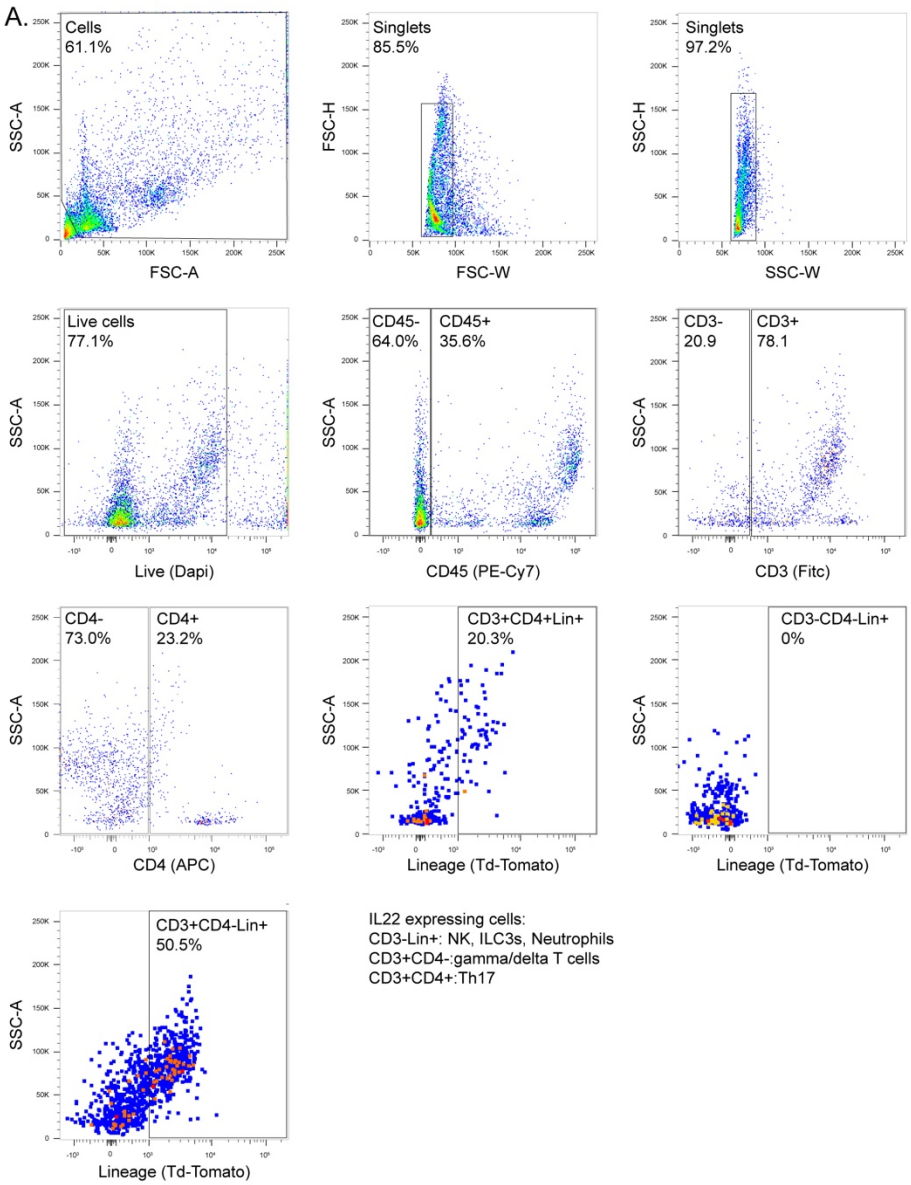

A.

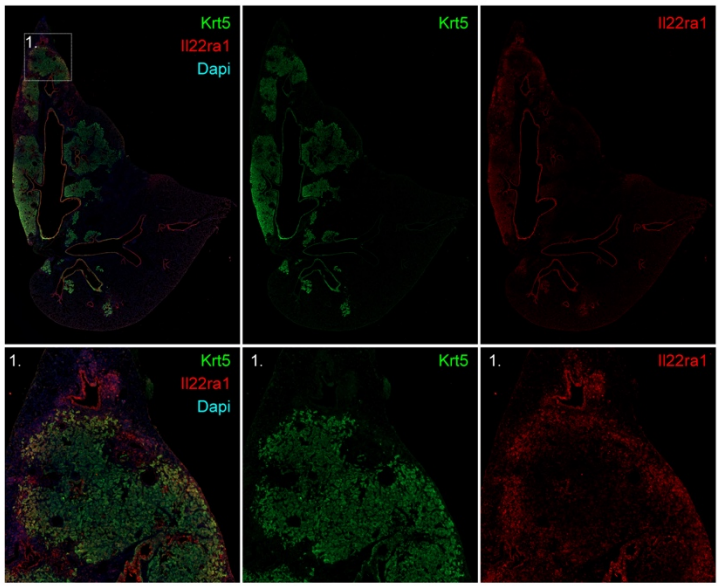

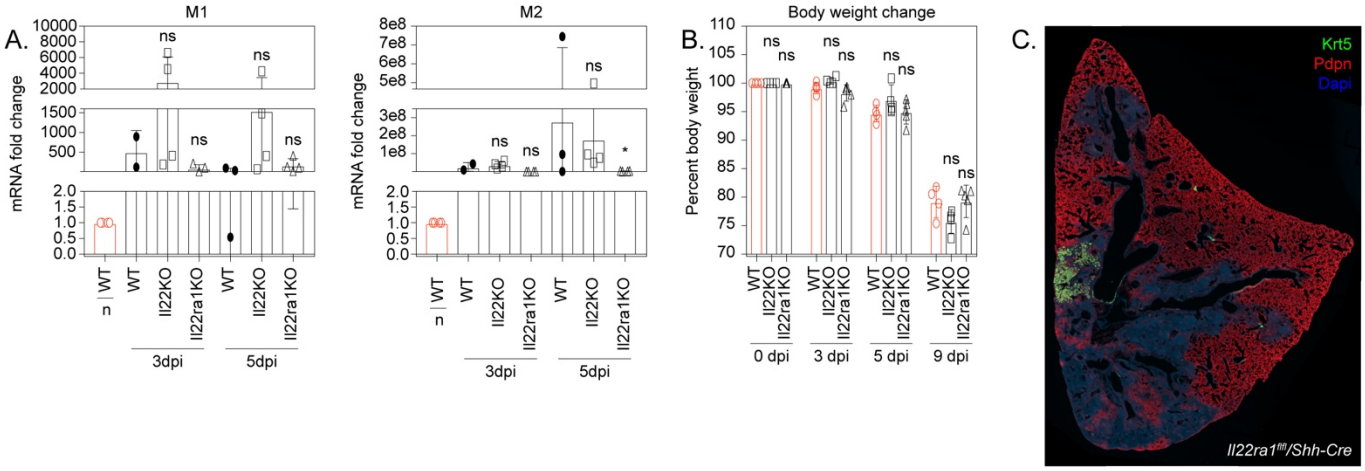

RESOURCE AVAILABILTY

Lead Contact:

Barry R. Stripp, Ph.D.

Cedars-Sinai Medical Center 8700 Beverly Blvd. AHSP Rm A9401 Los Angeles, CA 90048

E-mail: barry.stripp@cshs.org

Materials availability:

All unique/stable reagents generated in this study are available from the Lead Contact with a completed Materials Transfer Agreement.

Data and Code availability:

The data discussed in this publication have been deposited in NCBI's Gene Expression Omnibus (Edgar et al., 2002) and are accessible through GEO Series accession number GSE184384 (https://www.ncbi.nlm.nih.gov/geo/query/acc.cgi?acc=GSE184384).

EXPERIMENTAL MODEL AND SUBJECT DETAILS

Mouse strains:

Mice aged 8-12 weeks were used according to Institutional Animal Care and Use Committee-approved protocols. *Sftpc-CreER* (Rock et al., 2011), *Scgb1a1-CreER* (Rawlins et al., 2009),*Krt5-CreER* (Van Keymeulen et al., 2011), *IL-22*^{Cre} mice (Ahlfors et al., 2014), and *Shh-Cre* (Harfe et al., 2004) were obtained from Jackson Labs. *IL-22ra1*$^{fl/fl}$ (Zheng et al., 2016) were provided by Jay Kolls. These mice were bred to either *ROSA-26-mTmG* (Muzumdar et al., 2007). *ROSA-26-tdTomato* (supplied by D. Jiang and P.W. Noble) or *RC::RLTG* (Plummer et al., 2015) mice for lineage-tracing experiments. *Scgb3a2-DreER* mice were generated by Jackson Labs using a CRISPR/Cas9 knock-in strategy. Mice were produced by inserting an IRES-DreERT2 construct into the 3' UTR of the mouse *Scgb3a2* gene resulting in TM inducible DRE recombinase activity under the control of the *Scgb3a2* promoter. 4 Founders were identified following embryotic manipulation that carried the desired genetic permutation which was confirmed though long-range qPCR. Founders were back crossed to Bl6 mice to generate N1 progeny which were then bred to mice containing at least one copy of both *Scgb1a1-CreER* and *RC::RLTG* to generate the first generation of experimental mice for in vivo fate mapping experiments. For all experiments, 8-12 week-old mice were used and both male and female were included.

METHOD DETAILS

Tamoxifen & Influenza Virus inoculation:

Tamoxifen (TM) was dissolved by sonication at a concentration of 20mg/ml in corn oil that was stored at -80^{o}C in 50ml aliquots. Tracer mice were injected intraperitoneally using a 27 gauge needle 3 times

at a dose of 9mg/40g mouse body weight. TM treatment was performed 14 days prior to initial infection with influenza to provide enough washout time and, by extension, prevent residual TM activity prior to influenza infection. A mouse-adjusted variant of the 1918 H1N1 influenza was used to induce acute lung injury. A single treatment of 100PFU/50ul was administered intratracheally into isoflurane-sedated mice. Mouse weight was monitored over a 14-day period to verify proper infection has occurred. Whenever possible, the level of viral genes transcripts, M1 & M2, were also assessed from lung homogenate to further confirm that a reproducible level of infection has occurred in all conditions. Mouse lung biopsies were collected at time points that correspond with progression of basal pod formation in influenza infected mice.

Preparation of single cell suspensions for Single cell RNAseq:

Type II & immune subsets: Mouse lung biopsies were collected at the indicated time points: naïve, 3, 5, 7, 9, 11, 14, 17, 21, 60, 120 and 240 days post infection. A sample size of 5 C57/Bl6 WT mice were used for each timepoint. Cell suspensions from each condition were pooled together prior to cell sorting. On the day of biopsy collection, the entire mouse lung was separated from the chest cavity and stored in a conical containing 4^{o} C 1xHBSS. Isolated lung lobes were intratracheally instilled with a 3ml mixture containing 1U elastase/1ml 1xHBSS for 30 minutes at 37^{o} C. The crude cell suspension then underwent mechanical agitation before undergoing an additional incubation in dissociation solution containing 1x Liberase/1xHBSS for 30 minutes at 37^{o}C. Dissociation buffer was quenched with a solution containing 2%FBS/1mM EDTA/1X HBSS on ice. Cells were filtered through a 70µm nylon mesh to remove undigested tissue. Cells were centrifuged at 500g for 10 minutes and resuspended in 1ml blood cell lysis solution for 1 minute to remove red blood cells from the suspension. Red blood cell lysis buffer was quenched using 25 ml 2%FBS/1mM EDTA/1X HBSS and the cells underwent an additional centrifugation at 500g for 10 minutes. Cells were resuspended in 1ml 2%FBS/1mM EDTA/1X HBSS and magnetic bed separation was performed to deplete unwanted cell types. The following suspensions were then enriched for epithelial and immune populations using antibody based FACS. Using this strategy CD326^{+}CD45^{-}CD31^{-} epithelial and CD326^{-} CD45^{+}CD31^{-} immune cells were isolated. A minimum of 50,000 epithelial cells and 100,000 immune cells were sorted for each timepoint.

Conducting airway subsets: Single-cell RNA seq data was also generated from cell suspensions that were enriched for conducting airway epithelium. The aforementioned cell suspension prep was performed on TM inoculated *Sftpc-CreER*/*ROSA-mTmG* and a gating strategy was used to enrich for tdT negative epithelium (i.e. CD326^{+}CD45^{-}CD31^{-}tdT^{-}) using cell sorting. For these experiments, a sample size of 3 *Sftpc-CreER*/*ROSA-mTmG* were pooled together prior to cell sorting. Cells were collected at the same indicated time points (naïve, 3, 5, 7, 9, 11, 14, 17, 21, 60, 120 and 240 days post infection) and a minimum of 50,000 cells were collected per timepoint.

Conducting airway subsets (alternative): In experiments where isolation of conducting airway epithelium was not possible using *Sftpc-CreER*/*ROSA-mTmG* (Fig. 6.) an alternative gating strategy was used to deplete for Type II cells. In these experiments, a combination of Sca-1 and CD24 antibodies were used in lieu of the tdT lineage tag (i.e $CD326^{+}CD45^{-}CD31^{-}Sca1^{-}CD24^{-}$).

Bioinformatics analysis of flu single cell data:

Dataset Generation and gene expression analysis: Cell capture and cDNA library preparation was performed using reagents and a standardized workflow provided by 10x genomics (gene expression V2 & V3). A target capture of 3000 cells was performed for each timepoint. Novaseq S4 150 and 28+90 bp paired-end runs were outsourced to three separate institutions: UCLA genomics core, Novagene, Fulgent. Target read depth for V2 and V3 Kits was 50,000 and 20,000 reads per cell respectively. After generation of fastq files, alignment was performed on Cedars Sinai's high-performance cluster using a standard reference transcriptome provided by 10x genomics (refdata-cellranger-mm10-3.0.0). Aligned datasets were then pipelined into R studio and the R package "Seurat" (Butler et al., 2018; Stuart et al., 2019) was used to apply standard quality control metrics. Specifically, this was done to filter out dead cells (evidenced by cells with high mitochondrial gene content), to only include cells with unique molecular features, and to computationally regress out technical batch effect associated with separate capture runs. After QC metrics have been applied, unsupervised clustering was performed to cluster cells based molecular phenotype. Clusters that failed to show any pertinent difference in transcriptional signature were clustered together. Differential gene expression analysis was performed on each cluster to generate a gene list per cluster and cross referenced with gene signatures of these niches established within peer reviewed literature. After confirmation of a cell-type specific signature and unique molecular profile, the generated gene list was used to re-annotate pre-existing and subsequent datasets using the package singleR (Aran et al., 2019). All analysis relating to changes in transcript expression were performed using Seurat.

Secondary analysis pipelines: The R package "FGSEA" (Korotkevich et al., 2021) was used to perform gene set enrichment analysis. Single cell datasets were subsetted based on cell type and changes in gene expression was assessed at different points during flu infection using the hallmark gene sets from the molecular signature database(Liberzon et al., 2015; Subramanian et al., 2005). The R package "Velocyto" (La Manno et al., 2018) was used to perform the single cell trajectory analysis. Fastq files were realigned to a separate reference transcriptome containing both splice and unspliced variants of each gene. Before calculating RNA velocity, cell types of interest were subsetted from the compiled epithelial dataset and further subsetted based on timepoint. This was primarily done to reduce the computation required by the Velocyto package as well as to reduce potential for contaminating cell types becoming confounding factors. Degree node centralities were calculated from gene regulatory networks generated by the package "Bigscale2" (Iacono et al., 2018).

The “Bigscale2” package also has functionality to calculate difference in node centralities between two conditions. This function was used to generate a ranked list of the top 300 delta degree node centralities between early and late infection. The resultant rank list was used to assess enriched GO terms using a PANTHER based over-representation test produced by the gene ontology consortium (Ashburner et al., 2000; Gene Ontology, 2021; Mi et al., 2013). Gene networks were visualized using Cytoscape_v3.8.1.

Spatial transcriptomics expression analysis. Frozen 10µm sections from 14 days post PR8 infected mouse lungs were placed within the frames of the capture areas on the active surface of the Visium spatial slide. Tissue sections were fixed in methanol and stained with H&E. Bright-field images of stained sections in the fiducial frames were collected in 40× fields using Zeiss Axioscan Z1 microscopy. Stained tissue sections were permeabilized for 30 minutes and mRNA was released to bind oligonucleotides on the capture areas followed by reverse transcription, second strand synthesis, denaturation, cDNA amplification, and SPRIselect cDNA clean up, and then the cDNA libraries were prepared and sequenced on an Illumina NovaSeq SP with 28 bp + 90 bp paired-end sequencing mode. Mapping and counting were performed using Space Ranger 1.0.0 with the reference genome mmu10 provided by 10× Genomics. After mapping of the samples by Space Ranger, the data were processed in Seurat. The data were normalized by SCTransform and merged to build a unified UMAP. Seurat was used to transfer cluster labels from scRNASeq to spatial transcriptomic spots. The integrated mouse scRNASeq clusters were transferred to spatial transcriptomic sample. The transfer procedure generates a probability score for each spot and its association with a given scRNASeq cluster. The spot is assigned to the cluster with the highest score and mapped back to the spatial transcriptomic sample image.

Immunofluorescent microscopy:

Immunofluorescence staining: To prepare mouse lung for histology, we inflation fixed freshly dissected mouse lung through instillation of 1ml 4% paraformaldehyde directly into a cannulated mouse trachea. After incubating the lungs for 24 hours, the left lobe from each mouse was separated into a labeled cassette and stored in either 1x PBS for immediate tissue processing or in 70% EtOH for long term storage. Tissues were dehydrated using the ASP300 tissue processor(Leica). After processing, left lobes were embedded in paraffin wax and sectioned at 7-9µm thickness using a HM 325 rotary microtome(Leica). Sectioned slides were dried at room temperature until needed. After selection of an appropriate panel, tissue sections were deparaffinized using the Shandon veristain Gemini ES (Thermofisher, cat:A7800013). Slides were transferred into a reservoir containing either citrate or tris-based antigen retrieval solution(vector labs, cat:3300/3301) and heated using a pressure cooker (Biovendor, cat:RR2100-EU). The slides were then blocked with 2% bovine serum albumin for 30 minutes. Tissue sections were incubated in primary antibody overnight at 4^{o}C.

Following overnight incubation, cells were washed 5 times with 1x PBS and incubated in solution containing both alexaflour conjugated secondary antibody and DAPI for 2 hours. Slides were cover-slipped using Fluromount-G (EMS, cat:7984-25). Images were taken using either Zeiss 780 confocal microscope or the Zeiss Axioobserver Z1 inverted microscope.

Following are primary antibodies used: Chicken polyclonal anti-eGFP (1:1000, Abcam, Ab13970); Chicken Polyclonal anti-Keratin 5 (1:500, BioLegend, 905901); Mouse monoclonal anti-eGFP AF488 conjugated (1:500, Santa Cruz, Sc-9996); Rat monoclonal anti- IL-22ra1 (1:200, R&D systems, MAB42341); Goat polyclonal anti-tdTomato (1:500, Sicgen, Ab8181-200); Goat polyclonal anti-p63(1:500, Santa Cruz, Sc-8609); Goat Polyclonal UGRP1/SCGB3A2 (1:1000, R&D Systems, AF3465); Syrian hamster Monoclonal anti-Pdpn (1:1000, LifeSpan Biosciences, LS-C143022-100); Rabbit Polyclonal anti-SCGB1A1 (1:500, Proteintech, 10490-1-AP); Rabbit Polyclonal anti-RFP(1:500, Rockland, 600-401-379); Rabbit Polyclonal anti-Msln (1:500, Thermo Fisher Scientific, PA5-79698); Rabbit Polyclonal anti-Ltf (1:200, Thermo Fisher Scientific, PA5-95513); Rabbit Polyclonal anti-Bpifa1 (1:200, Sigma-Aldrich, AV42475); Rabbit polyclonal anti-Keratin 5 (1:500, Cell Marque, EP1601Y); Rabbit polyclonal anti-Keratin 5 (1:500, Santa Cruz, Sc-66856); Rabbit polyclonal anti IL-22 (1:200, Abcam, ab18499); Rabbit polyclonal anti-Ki67 (1:1000, Ebioscience, 14-5698-82).

Following are secondary antibodies used: Goat anti-Chicken Alexa Fluor 488(1:500, Thermo Fisher Scientific, 6100-30); Goat anti-Hamster Alexa Fluor 488 (1:500, Thermo Fisher Scientific, A-21110); Donkey anti-Rabbit Alexa Fluor 488 (1:500, Thermo Fisher Scientific, A-21206); Donkey anti-Goat Alexa Fluor 555(1:500, Thermo Fisher Scientific, A-21432); Donkey anti-Rabbit Alexa Fluor 555 (1:500, Thermo Fisher Scientific, A-31572); Goat anti-Chicken Alexa Fluor 568 (1:500, Thermo Fisher Scientific, A-11041); Donkey anti-Rat Alexa Fluor 594(1:500, Thermo Fisher Scientific, A-21209); Goat anti-Hamster Alexa Fluor 594 (1:500, Thermo Fisher Scientific, A-21113); Goat anti-Chicken Alexa Fluor 647 (1:500, Thermo Fisher Scientific, A-21449); Donkey anti-Rabbit Alexa Fluor 647 (1:500, Thermo Fisher Scientific, A-31573); Donkey anti-Goat Alexa Fluor 647 (1:500, Thermo Fisher Scientific, A-31573); Donkey anti-Goat Alexa Fluor 647 (1:500, Thermo Fisher Scientific, A-21447).

Lineage tracing analysis:

Quantification of cells per unit BM: To score the number of cells per unit BM, 20 lines along the basement membrane was measured using the “segmented line tool” in the Fiji image analysis software(Schindelin et al., 2012) and recorded into a google spreadsheet. The number of lineage tagged tdT and eGFP tagged populations from the Scgb1a1/Scgb3a2 dual tracers was counted along a basement membrane length of 300μm. Three regions of interest were selected from intrapulmonary conducting airway epithelium per biological replicate. A biological sample size of 3 was used for all conditions.

Quantification of Pod region percent totals: Pods were defined as at least five continuous Krt5/eGFP/tdT$^-$immunostained cells in alveolar regions that were not associated with pre-existing bronchial epithelium. 100 pod cells per region of interest were counted using Fiji's "multi-point" function and recorded into a google spreadsheet. Then the percentage of either tdT low, tdT high or eGFP positive cells were assessed based on the function of counted pod cells. Three regions of interest were selected from each pod region per biological replicate. A biological sample size of 3 was used for all experiments.

Quantification of Krt5 area in *IL-22^{Cre}* and *IL-22ra1$^{fl/fl}$/Shh-Cre*:

Quantification of Krt5 area was calculated by measuring the area of Krt5 immunostained pods in proportion to the area of damaged regions demarcated by DAPI$^+$PDPN$^-$ stain within alveolar epithelium using Fiji software. Imported images were separated by channel and converted into greyscale using the following sequence of image processing features: Image -> Type -> 8bit. Area's containing positive stain were then converted into binary black/white images using the following sequence of images processing features: Process -> Binary-> Make Binary. Area of each channel was measured and recorded into a google spreadsheet using the following sequence of features: Analyze -> Analyze particles.

Quantitative real-time PCR

RNA was extracted from homogenized snap frozen superior lobes of either *IL-22^{Cre}* homozygous, *IL-22ra1$^{fl/fl}$/Shh-Cre* or WT controls using RNAeasy mini kit(Qiagen, cat: 74106). Isolated RNA was converted into cDNA using a iScript cDNA synthesis kit (Bio-Rad, cat:1708891). Gene expression analysis was performed using SYBR Green PCR master Mix (Thermo Fisher Scientific, cat: 4309155)and analyzed on the 7500 fast Real-Time PCR system (Thermo Fisher Scientific). Between 3-5 isolated superior lobes were analyzed per condition.

Flow cytometry of IL-22 expressing cells:

IL-22^{Cre} homozygous mice were purchased and bred to heterozygosity with another strain expressing at least one copy of *ROSA-tdT* to generate *IL-22^{Cre}/ROSA-tdT* mice. Mouse lungs were collected from steady state and from mice infected with influenza for 14 days. At indicated time points, mouse lung was collected and processed into single cell suspension as described above. An immune panel capable of delineating between T helper and non-T-helper subsets (CD3$^+$CD4$^+$ and CD3$^+$CD4$^-$ respectively) was used to determine the main IL-22 expressing cells using flow cytometry.

Multiplex protein assays:

Mouse bronchial alveolar lavage (BAL) and mouse left lobes were collected at the following time points: naïve, 3, 5, 7, 9, 11, 14 , 17, 21dpi. BAL was prepared through instillation of intubated mouse trachea with 1ml 1x dPBS three times. Instilled dPBS was transferred into a 1.5 microfuge tube. To prepare lung homogenates, dissected lobes were transferred into collection tubes containing 1.4 mm

ceramic beads(Lysing matrix D, MP Biomedicals Cat: 116913100) and homogenized using mechanical agitation(MP Benchtop Homogenizer, MP biomedicals, Cat: 6VFV9). Samples were centrifuged at 600rcf to pellet cells. Supernatants were transferred into a separate 1.5mL collection tube. A multiplexed protein assay (Bio-plex Pro, Bio-Rad, Cat: 171304070 , M69999997NY) was performed to assess changes in expression of the following cytokines: IL-1b, IL-6, IL-10, IL-17, IL-22, Tnfα and Ifnγ. Samples were processed for analysis as per manufactures instructions. Cytokine levels were quantified using the fluid flow-based microplate reader (Bio-plex 200, Luminex ,Cat:171000201).

QUANTIFICATION AND STATISTICAL ANALYSIS

Detailed descriptions relating to quantification and statistical analysis of each experiment is documented in the above Methods section. Statistical analysis from graphs generated by wet lab experiments was performed in Graphpad Prism 7. Variance in datapoints between conditions is represented by Mean +/-SEM. Statistical analysis for single cell RNA seq data was performed using pipelines for statistical analysis inherit to each package.

ADDITIONAL RESOURCES

KEY RESOURCES TABLE

REAGENT or RESOURCE	SOURCE	IDENTIFIER
Antibodies		
Primary antibodies for IF:		
Chicken polyclonal anti-eGFP	Abcam	Ab13970
Chicken Polyclonal anti-Keratin 5	BioLegend	905901
Mouse monoclonal anti-eGFP AF488	Santa Cruz	Sc-9996
Rat monoclonal anti-IL-22ra1	R&D systems	MAB42341
Goat polyclonal anti-tdTomato	Scigen	Ab8181-200
Goat polyclonal anti-p63	Santa Cruz	Sc-8609
Goat Polyclonal Ugrp1/Scgb3a2	R&D Systems	AF3465
Syrian hamster Monoclonal anti-Pdpn	LifeSpan Biosciences	LS-C143022-100
Rabbit Polyclonal anti-Scgb1a1	Proteintech	10490-1-AP
Rabbit Polyclonal anti-RFP	Rockland	600-401-379
Rabbit Polyclonal anti-Msln	Thermo Fisher Scientific	PA5-79698
Rabbit Polyclonal anti-Ltf	Thermo Fisher Scientific	PA5-95513
Rabbit Polyclonal anti-Bpifa1	Sigma-Aldrich	AV42475
Rabbit polyclonal anti-Keratin 5	Cell Marque	EP1601Y
Rabbit polyclonal anti-Keratin 5	Santa Cruz	Sc-66856
Rabbit polyclonal anti IL-22	Abcam	ab18499
Rabbit polyclonal anti-Ki67	ebioscience	14-5698-82
Secondary antibodies for IF:		
Goat anti-Chicken Alexa Fluor 488	Thermo Fisher Scientific	6100-30
Goat anti-Hamster Alexa Fluor 488	Thermo Fisher Scientific	A-21110
Donkey anti-Rabbit Alexa Fluor 488	Thermo Fisher Scientific	A-21206
Donkey anti-Goat Alexa Fluor 555	Thermo Fisher Scientific	A-21432

Donkey anti-Rabbit Alexa Fluor 555	Thermo Fisher Scientific	A-31572
Goat anti-Chicken Alexa Fluor 568	Thermo Fisher Scientific	A-11041
Donkey anti-Rat Alexa Fluor 594	Thermo Fisher Scientific	A-21209
Donkey anti-Goat Alexa Fluor 594	Thermo Fisher Scientific	A-11058
Donkey anti-Rabbit Alexa Fluor 594	Thermo Fisher Scientific	A-21207
Goat anti-Hamster Alexa Fluor 594	Thermo Fisher Scientific	A-21113
Goat anti-Chicken Alexa Fluor 647	Thermo Fisher Scientific	A-21449
Donkey anti-Rabbit Alexa Fluor 647	Thermo Fisher Scientific	A-31573
Donkey anti-Goat Alexa Fluor 647	Thermo Fisher Scientific	A-21447
Primary antibodies for Flow:		
Fitc rat monoclonal anti-CD45	BioLegend	103108
Fitc rat monoclonal anti-CD31	BioLegend	102406
APC rat monoclonal anti-CD326	BioLegend	118218
Pe/Cy7 rat monoclonal anti-CD326	BioLegend	118216
Biotin monoclonal anti-CD31	BioLegend	102404
Biotin monoclonal anti-CD45	BioLegend	103104
Biotin monoclonal anti-Ly-6A/E	BioLegend	108112
Bacterial and virus strains		
Influenza A virus (H1N1)	ATCC	VR-95
Chemicals, peptides, and recombinant proteins		
Antigen Unmasking Solution, Tris-Based	Vector Laboratories	H-3301
Antigen Unmasking Solution, Citric Based	Vector Laboratories	H-3300
Tamoxifen, ≥99%	Sigma-Aldrich	T5648-5G
Elastase	Worthington Biochemical	LS002280
Liberase™ TM Research Grade	Sigma-Aldrich	5401127001
1X RBC Lysis Buffer	eBioscience	00-4333-57
Critical commercial assays		
Lysing matrix D 2 mL tubes	MP Biomedicals	116913100
Bio-plex 200	Luminex	171000201
Bio-plex Pro 6-plex	Bio-Rad	171304070
Bio-plex Pro 1-plex (custom)	Bio-Rad	M69999997NY
MP Benchtop Homogenizer	MP Biomedicals	6VFV9
RNAeasy mini kit	Qiagen	74106
IScript cDNA synthesis kit	Bio-Rad	1708891
SYBR Green PCR master Mix	Thermo Fisher Scientific	4309155
Deposited data		
Raw and analyzed data	This manuscript	GSE184384
Experimental models: Organisms/strains		
Sftpc-CreER	Source: Jackson Labs; (Rock et al., 2011)	028054
Scgb1a1-CreER	Source: Jackson Labs; (Rawlins et al., 2009)	016225
Krt5-CreER	Source: Jackson Labs; (Van Keymeulen et al., 2011)	029155
IL-22^{Cre}	Source: Jackson Labs; (Ahlfors et al., 2014)	027524

IL-22ra1$^{fl/fl}$	Source: Jackson Labs; (Zheng et al., 2016)	031003
Shh-Cre	Source: Jackson Labs; (Harfe et al., 2004)	005622
ROSA-26-mTmG	Source: Jackson Labs; (Muzumdar et al., 2007)	007576
ROSA-26-tdT	Source: collaborator; (Madisen et al., 2010)	007905
RC::RLTG	Source: Jackson Labs;(Plummer et al., 2015)	026931
Scgb3a2-DreER	Source: Jackson Labs	NA – novel line
Software and algorithms		
Fiji image analysis software	(Schindelin et al., 2012)	https://imagej.net/software/fiji/
Graphpad Prism7	GraphPad	https://www.graphpad.com/scientific-software/prism/
Illustrator	Adobe	https://www.adobe.com/products/illustrator.html
Zen2	Zeiss	https://www.zeiss.com/microscopy/us/products/microscope-software/zen.html